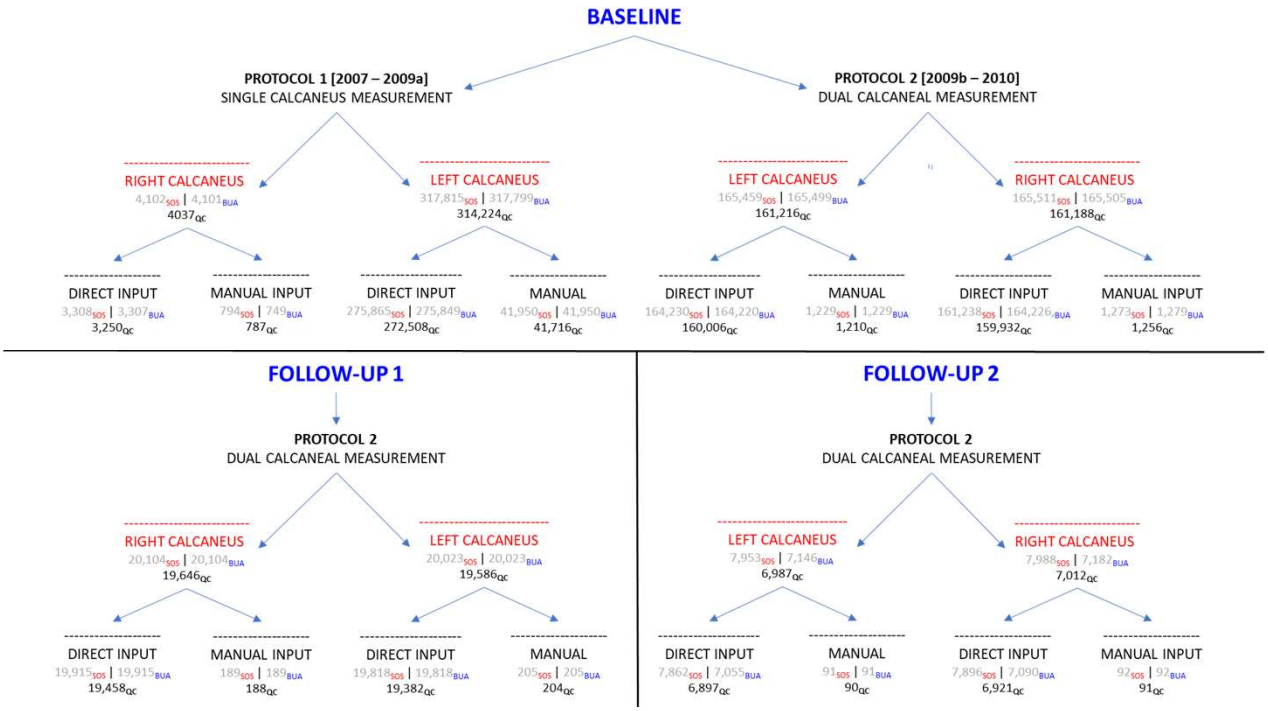

Supplementary Figure 1. Flow diagram illustrating calcaneal quantitative ultrasound (QUS) data collection by the UK Biobank. QUS data were collected at three time points: Baseline (2007 to 2010), Follow-up 1 (2012 to 2013) and Follow-up 2 (2014 to 2016). At baseline, QUS was performed using two protocols (denoted protocol 1 and 2). Protocol 1 was implemented from 2007 to mid-2009 and involved measuring the left calcaneus. Only in cases where the left was missing or deemed unsuitable was the right calcaneus measured. Protocol 2 was introduced from mid-2009, (replacing protocol 1) and differed only in that it involved measuring both the left and right calcanei. Protocol 2 was further used for both follow up assessments. For all three time points, calcaneal QUS was performed with the Sahara Clinical Bone Sonometer [Hologic Corporation (Bedford, MA, USA)]. Vox software was used to automatically collect data from the sonometer (denoted direct input). In cases where direct input failed, QUS outcomes were manually keyed into Vox by the attending healthcare technician or nurse (i.e. manual input). The number of individuals with non-missing measures for speed of sound (SOS) and broadband ultrasound attenuation (BUA) recorded at each assessment period are indicated in light grey. Further details on these methods are publicly available on the UK Biobank website (UK Biobank document #100248, "URLs"). To reduce the impact of outlying measurements, Individuals with highly discordant left versus right calcaneal measures were excluded from the analysis. Furthermore, quality control was applied to male and female subjects separately using the following exclusion thresholds: SOS [Male: (≤1,450 and ≥1,750 m/s), Female (≤1,455 and ≥1,700 m/s)] and BUA [Male: (≤27 and ≥138 dB/MHz), Female (≤22 and ≥138 dB/MHz)]. Individuals exceeding the threshold for SOS or BUA or both were removed from the analysis. Estimated bone mineral density [eBMD, (g/cm2)] was derived as a linear

combination of SOS and BUA [eBMD=0.002592*(BUA+SOS)-3.687]. Individuals exceeding the following thresholds for eBMD were further excluded: [Male: (≤0.18 and ≥1.06 g/cm2), Female (≤0.12 and ≥1.025 g/cm2)]. The number of individuals with non-missing measures for SOS, BUA and eBMD after QC are indicated in black. A unique list of individuals with a valid measure for the left calcaneus (n=477,380) and/or right (n=181,953) were identified separately across all three time points. Individuals with a valid right calcaneus measure were included in the final data set when no left measures were available, giving a preliminary working dataset of n=481,100 (left=475,724 and right=5,376) unique individuals. Bivariate scatter plots of eBMD, BUA and SOS were visually inspected and 723 additional outliers were removed, leaving a total of 480,377 valid QUS measures for SOS, BUA and BMD (264,304 females and 216,073 males).

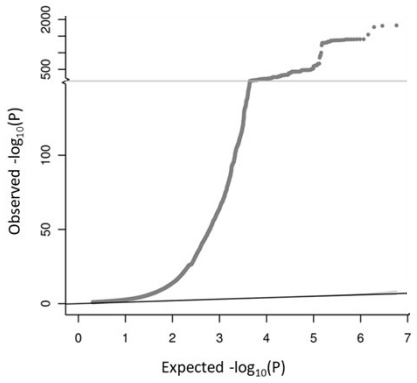

Supplementary Figure 2. QQ-plot of GWAS for eBMD in n=426,824 UK Biobank participants. Observed -$\log_{10}$ p-values were calculated from genome-wide non-infinitesimal mixed model association p-values estimated with BOLT-LMM (Loh *et al*. 2015, DOI: 10.1038/ng.3190).

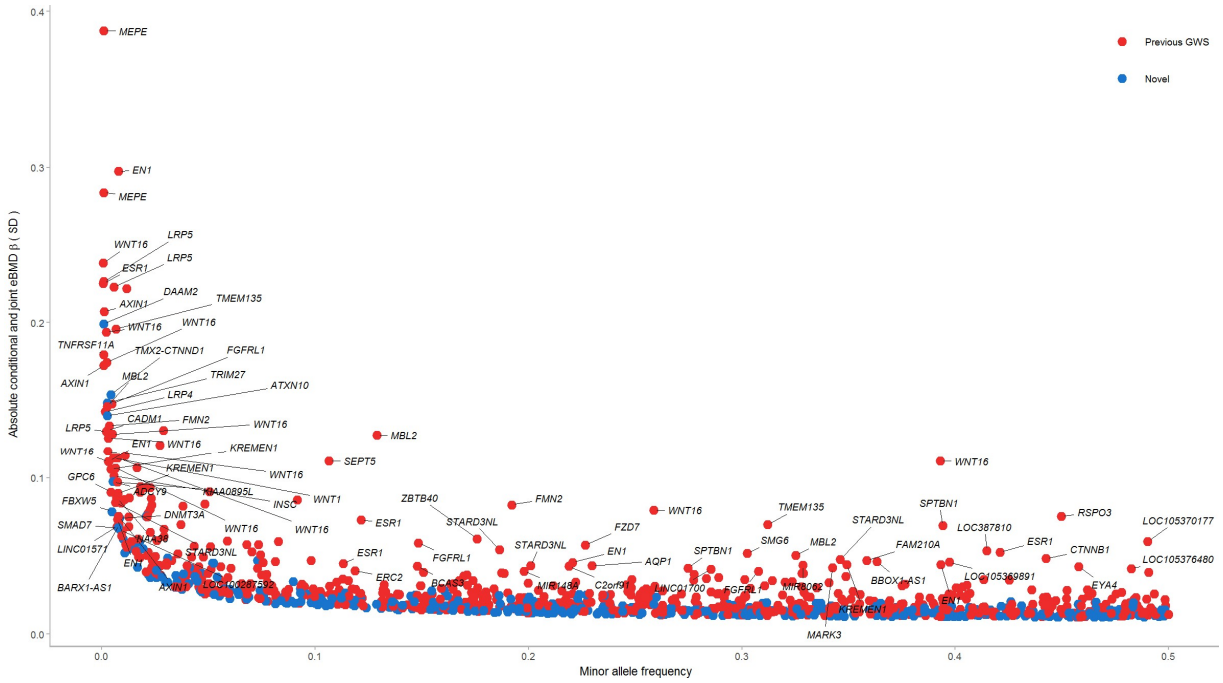

Supplementary Figure 3. Relationship between absolute effect size (y-axis) and minor allele frequency (x-axis) for 1,103 conditionally independent SNPs. Red dots represent SNPs at previously reported BMD loci. Blue dots represent SNPs at novel loci. The named gene is that closest to the SNP that has the smallest p-value of all conditionally independent SNPs [$p<6.6x10^{-9}$ after conditional independence testing using GCTA-COJO (Yang *et al.* 2011, DOI: 10.1016/j.ajhg.2010.11.011, Yang *et al.* 2012, DOI: 10.1038/ng.2213)] present in the same locus. We emphasize that proximity is not necessarily indicative of causality.

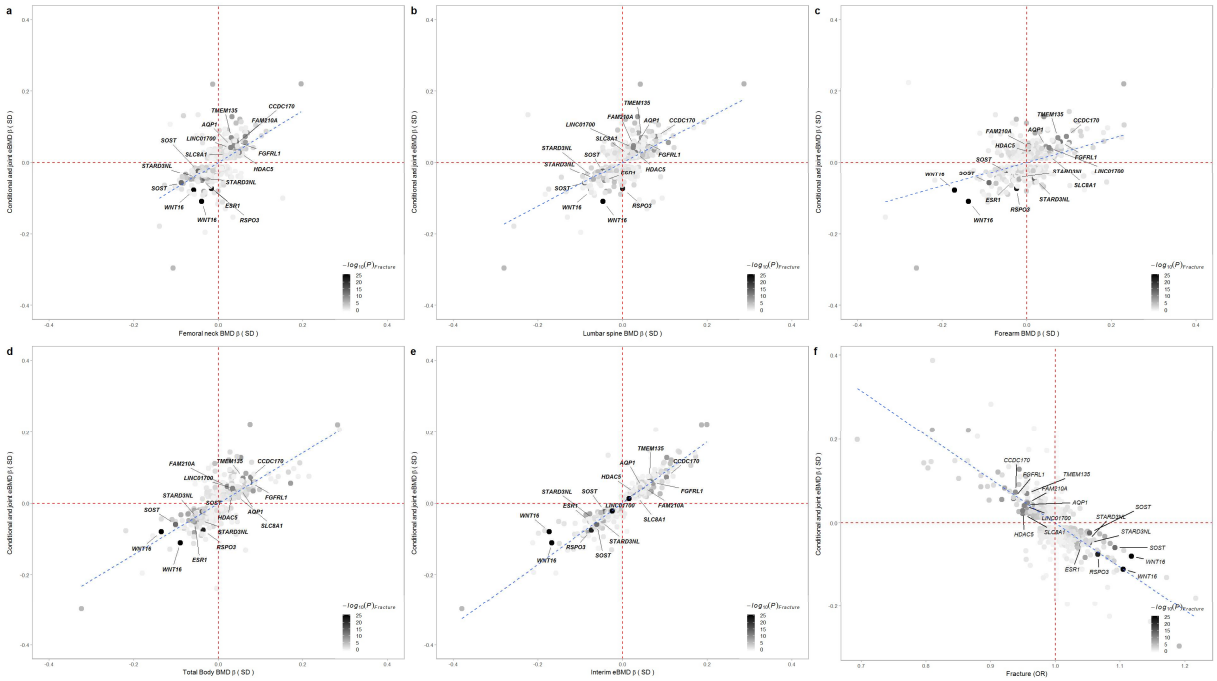

Supplementary Figure 4. Effect size in standard deviations for eBMD (y-axis) from the UK Biobank plotted against effect size in standard deviations from previous GEFOS studies for BMD at the (a) femoral neck, (b) lumbar spine, (c) forearm, (d) total-body, (e) heel and (f) fracture as per the full UK Biobank cohort (x-axis). 1,103 conditionally independent variants that reached genome-wide significance ($p<6.6 \times 10^{-9}$) for eBMD in n=426,824 UK Biobank participants were plotted. $-\log_{10}$ p-value for the fracture analysis in UK Biobank is represented by the shading of the data points (black for robust evidence of association with fracture and white for poor evidence of association). The blue dashed trend line shows a moderate to strong correlation between estimated effect sizes at the heel and femoral neck [n_{SNPs}=1,060, r=0.53 95%-CI (0.49,0.57)], lumbar spine [n_{SNPs}=1,075, r=0.59 (0.55,0.63)], forearm [n_{SNPs}=1,060, r=0.46 (0.41, 0.50)], total-body [n_{SNPs}=1,074, r=0.70 (0.67,0.73)], interim heel [n=1,079, r=0.93 (0.92,0.94)] and fracture [n=1,099, r=−0.77 (−0.79, −0.75)]. SNPs that reach genome-wide significance for fracture look-up ($p<6.6 \times 10^{-9}$) are labelled in black. Pearson product-moment correlation coefficients were used to describe the linear relationship between the standardized effect sizes.

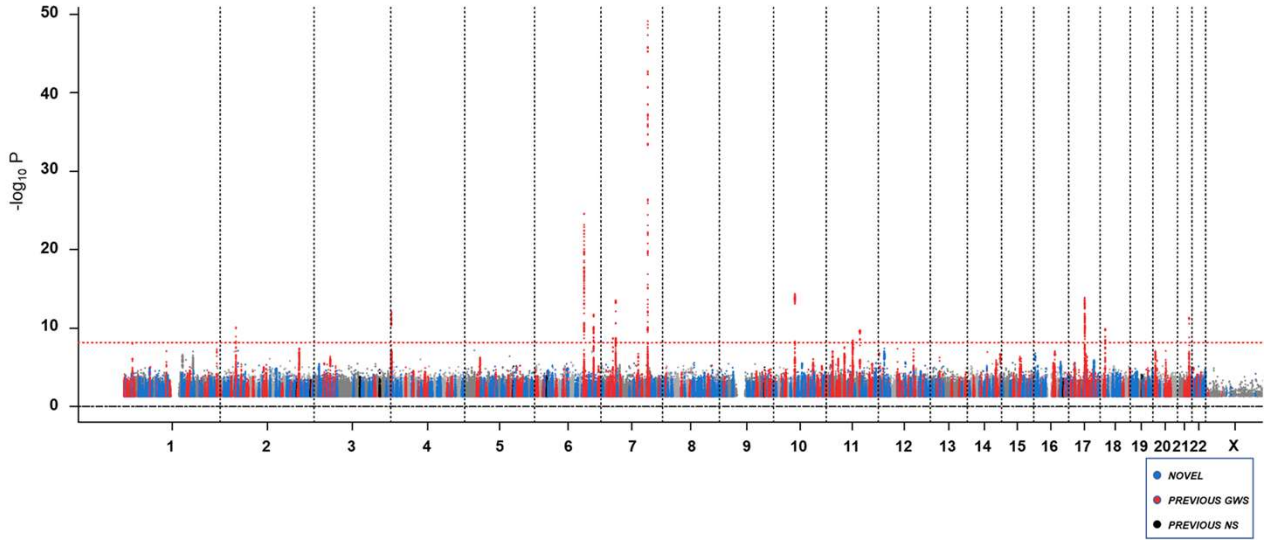

Supplementary Figure 5. Manhattan plot of genome-wide association results for fracture in the UK Biobank in n=426,795 (n_{cases}=53,184). Manhattan plot showing genome-wide association results for fracture in the UK Biobank. -$\log_{10}$ p-values were calculated from infinitesimal mixed model association p-values estimated with BOLT-LMM (Loh *et al*. 2015, DOI: 10.1038/ng.3190). The dashed red line denotes the threshold for declaring genome-wide significance (6.6×10^{-9}). In total, 14 conditionally independent SNPs, identified from conditional independence testing with GCTA-COJO (Yang *et al*. 2011, DOI: 10.1016/j.ajhg.2010.11.011, Yang *et al*. 2012, DOI: 10.1038/ng.2213), at 13 loci passed the criteria for genome-wide significance. Blue dots represent a locus identified from the eBMD GWAS that was novel in this analysis. Red dots represent a locus associated with eBMD which was known from previous studies. Previously reported BMD loci failing to reach genome-wide significance in our study are shown in black.

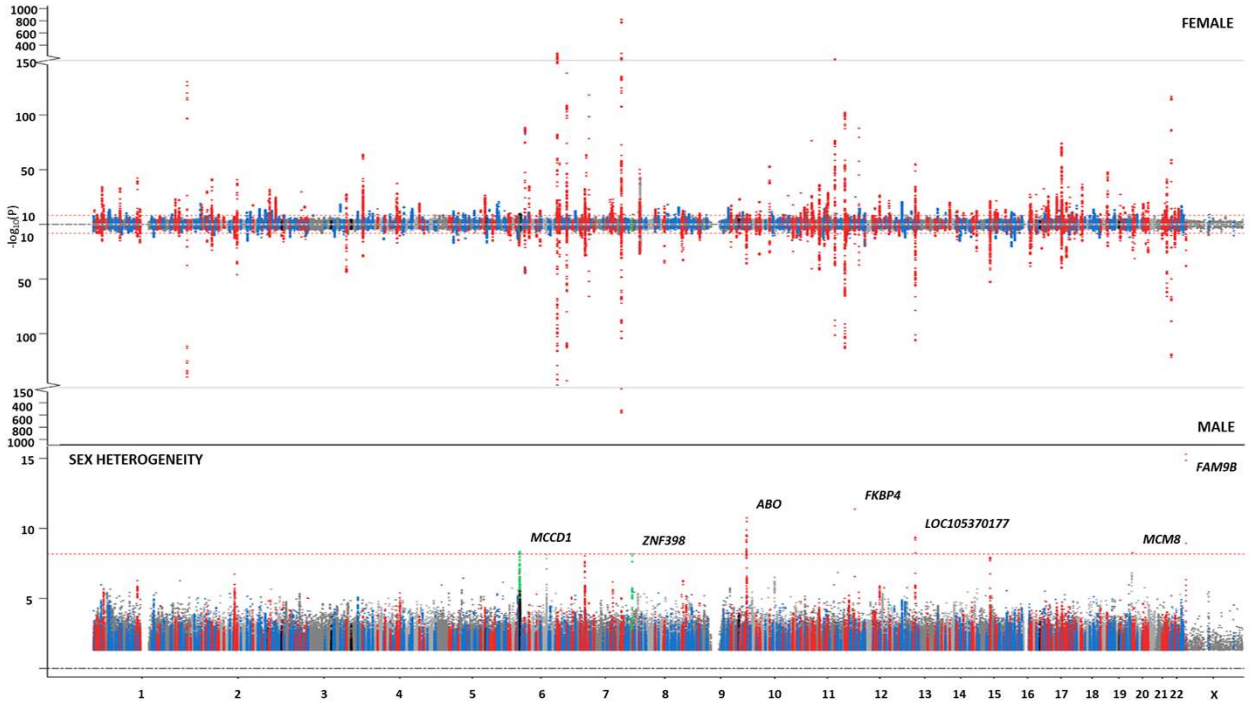

Supplementary Figure 6. Analysis of sex heterogeneity for eBMD. The top-most figure is a Miami plot of genome-wide association results for females (top panel) and males (bottom panel). The bottom graph is a Manhattan plot for the test for sex heterogeneity in eBMD regression coefficients between males and females. Previously reported loci that reached genome-wide significance ($p<6.6 \times 10^{-9}$) are displayed in red, and previously reported loci failing to reach genome-wide significance in our study are shown in black. Loci containing *ABO, FKBP4, LOC105370177* and *FAM9B* had stronger effects on eBMD in males, whereas *MCM8* had a larger effect in females. Loci demonstrating significant heterogeneity ($p<6.6 \times 10^{-9}$) but were not robustly associated at genome-wide significance with eBMD in the males and/or females are in green (i.e. *MCCD1* and *ZNF398*). Sample size by sex and total number of variants analyzed: Male=193,639, Female=233,185, #Vars=13,753,390. The statistical test is described in the **Supplementary Note**: Heterogeneity in effect size coefficients between sexes was tested in EasyStrata (Winkler *et al*. 2015, DOI: 10.1093/bioinformatics/btu621), using Cochran's test of heterogeneity.

a

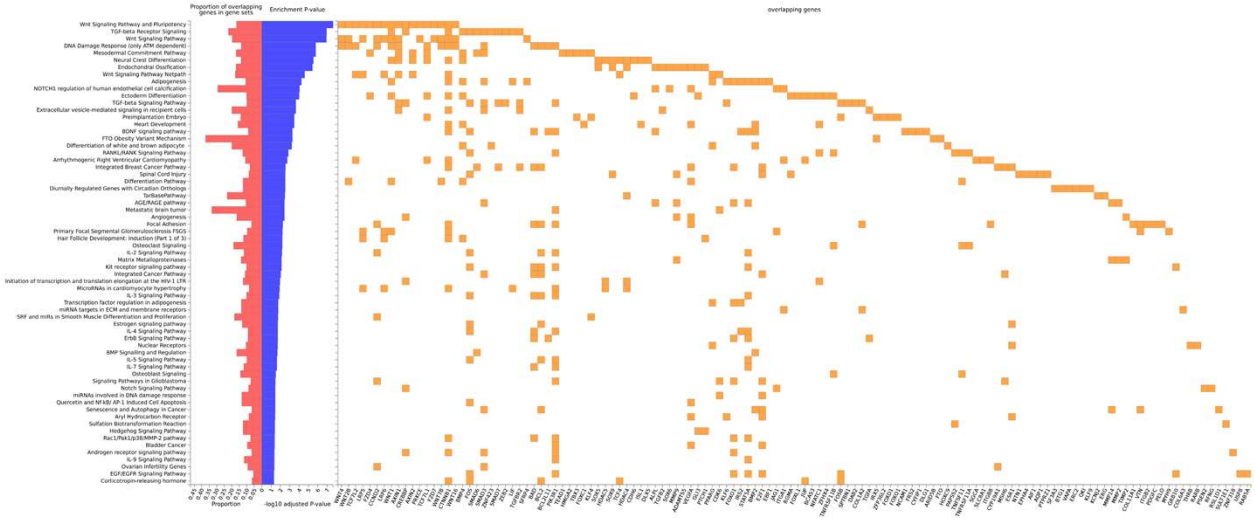

Supplementary Figure 7. WikiPathways pathway analysis results from FUMA (Watanabe *et al.* 2017, DOI: 10.1038/s41467-017-01261-5) hypergeometric testing. We tested enrichment for (**a**) genes closest to a fine-mapped SNP (n=538 genes), (**b**) genes with fine-mapped SNPs mapping to its gene body (n=287 genes), (**c**) genes with coding fine-mapped SNPs (n=39 genes), (**d**) genes mapped closest to a fine-mapped SNP which resided in an SaOS-2 ATAC-seq peak (n=62 genes), and genes identified by fine-mapped SNP was present in a (**e**) Hi-C osteoblast (n=54 genes) or (**f**) osteocyte (n=24 genes) promoter interaction peak. Well known pathways for bone biology were highlighted by FUMA, such as Wnt signalling, endochondral ossification, osteoclast and osteoblast signalling.

b

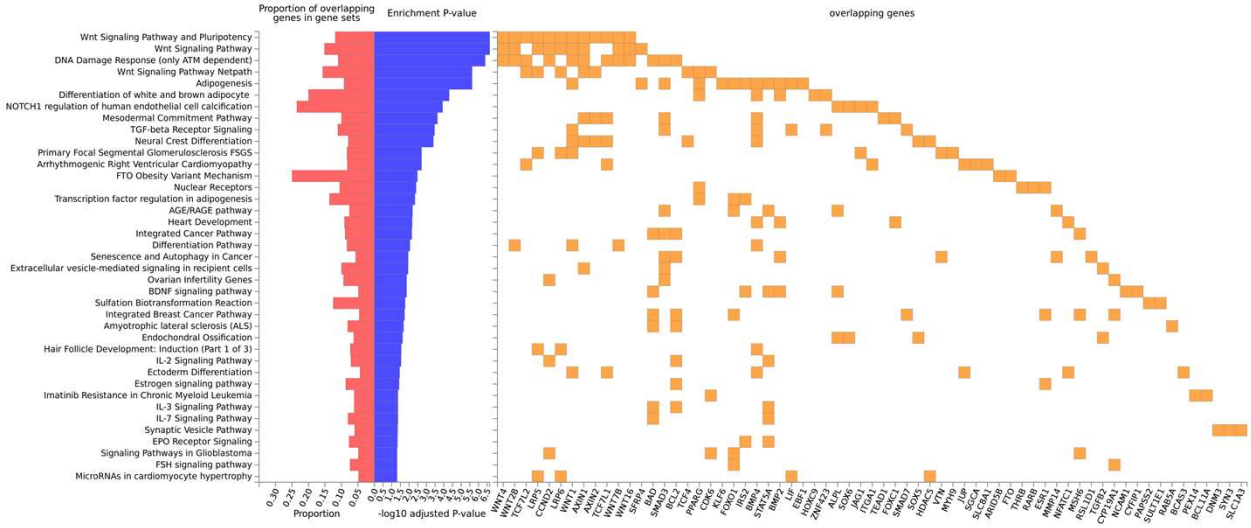

Supplementary Figure 7. WikiPathways pathway analysis results from FUMA (Watanabe *et al.* 2017, DOI: 10.1038/s41467-017-01261-5) hypergeometric testing. We tested enrichment for (**a**) genes closest to a fine-mapped SNP (n=538 genes), (**b**) genes with fine-mapped SNPs mapping to its gene body (n=287 genes), (**c**) genes with coding fine-mapped SNPs (n=39 genes), (**d**) genes mapped closest to a fine-mapped SNP which resided in an SaOS-2 ATAC-seq peak (n=62 genes), and genes identified by fine-mapped SNP was present in a (**e**) Hi-C osteoblast (n=54 genes) or (**f**) osteocyte (n=24 genes) promoter interaction peak. Well known pathways for bone biology were highlighted by FUMA, such as Wnt signalling, endochondral ossification, osteoclast and osteoblast signalling.

c

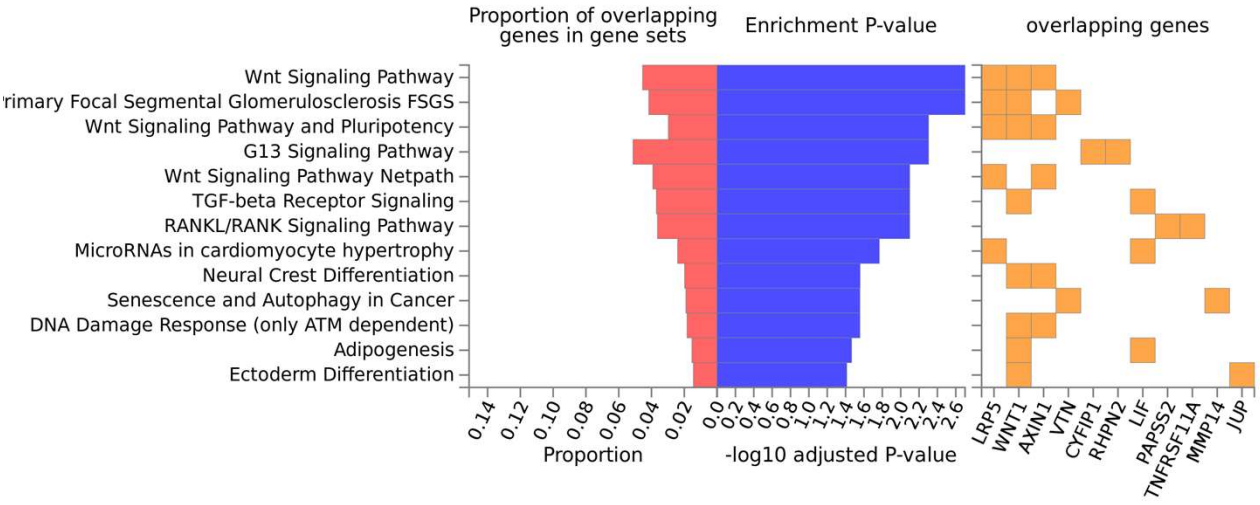

Supplementary Figure 7. WikiPathways pathway analysis results from FUMA (Watanabe *et al.* 2017, DOI: 10.1038/s41467-017-01261-5) hypergeometric testing. We tested enrichment for (**a**) genes closest to a fine-mapped SNP (n=538 genes), (**b**) genes with fine-mapped SNPs mapping to its gene body (n=287 genes), (**c**) genes with coding fine-mapped SNPs (n=39 genes), (**d**) genes mapped closest to a fine-mapped SNP which resided in an SaOS-2 ATAC-seq peak (n=62 genes), and genes identified by fine-mapped SNP was present in a (**e**) Hi-C osteoblast (n=54 genes) or (**f**) osteocyte (n=24 genes) promoter interaction peak. Well known pathways for bone biology were highlighted by FUMA, such as Wnt signalling, endochondral ossification, osteoclast and osteoblast signalling.

d

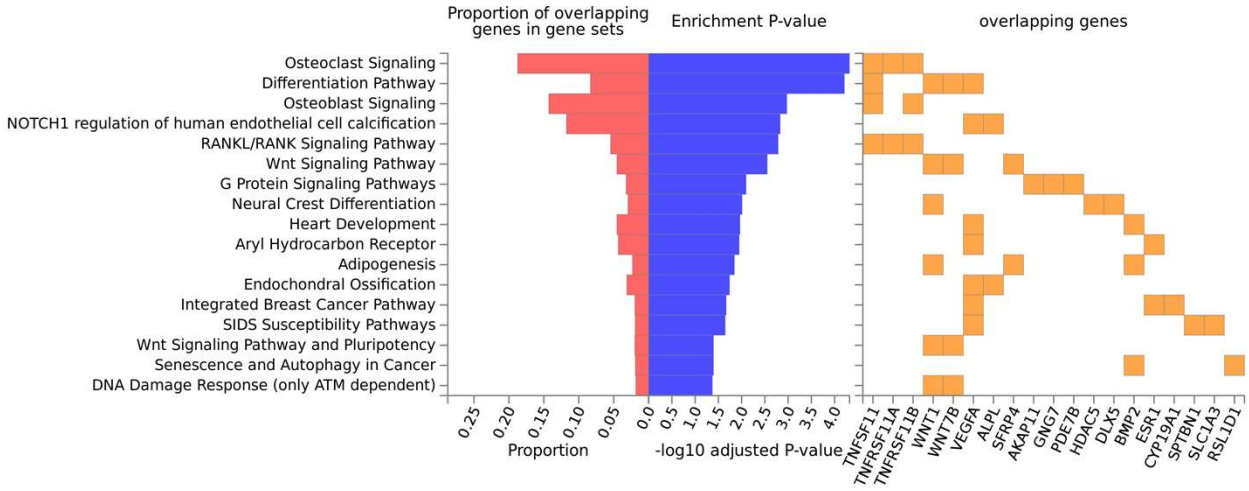

Supplementary Figure 7. WikiPathways pathway analysis results from FUMA (Watanabe *et al.* 2017, DOI: 10.1038/s41467-017-01261-5) hypergeometric testing. We tested enrichment for (**a**) genes closest to a fine-mapped SNP (n=538 genes), (**b**) genes with fine-mapped SNPs mapping to its gene body (n=287 genes), (**c**) genes with coding fine-mapped SNPs (n=39 genes), (**d**) genes mapped closest to a fine-mapped SNP which resided in an SaOS-2 ATAC-seq peak (n=62 genes), and genes identified by fine-mapped SNP was present in a (**e**) Hi-C osteoblast (n=54 genes) or (**f**) osteocyte (n=24 genes) promoter interaction peak. Well known pathways for bone biology were highlighted by FUMA, such as Wnt signalling, endochondral ossification, osteoclast and osteoblast signalling.

e

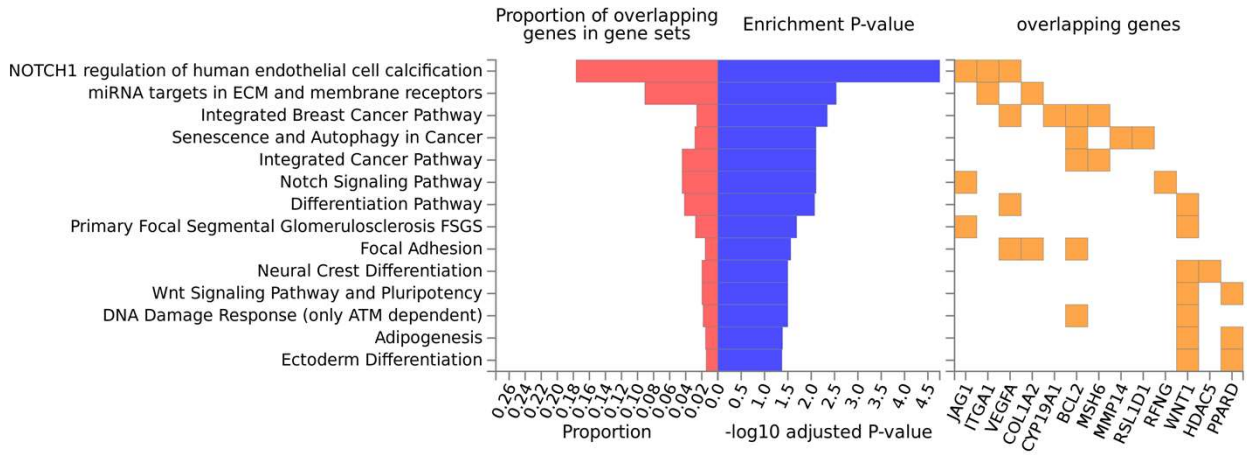

Supplementary Figure 7. WikiPathways pathway analysis results from FUMA (Watanabe *et al.* 2017, DOI: 10.1038/s41467-017-01261-5) hypergeometric testing. We tested enrichment for (**a**) genes closest to a fine-mapped SNP (n=538 genes), (**b**) genes with fine-mapped SNPs mapping to its gene body (n=287 genes), (**c**) genes with coding fine-mapped SNPs (n=39 genes), (**d**) genes mapped closest to a fine-mapped SNP which resided in an SaOS-2 ATAC-seq peak (n=62 genes), and genes identified by fine-mapped SNP was present in a (**e**) Hi-C osteoblast (n=54 genes) or (**f**) osteocyte (n=24 genes) promoter interaction peak. Well known pathways for bone biology were highlighted by FUMA, such as Wnt signalling, endochondral ossification, osteoclast and osteoblast signalling.

f

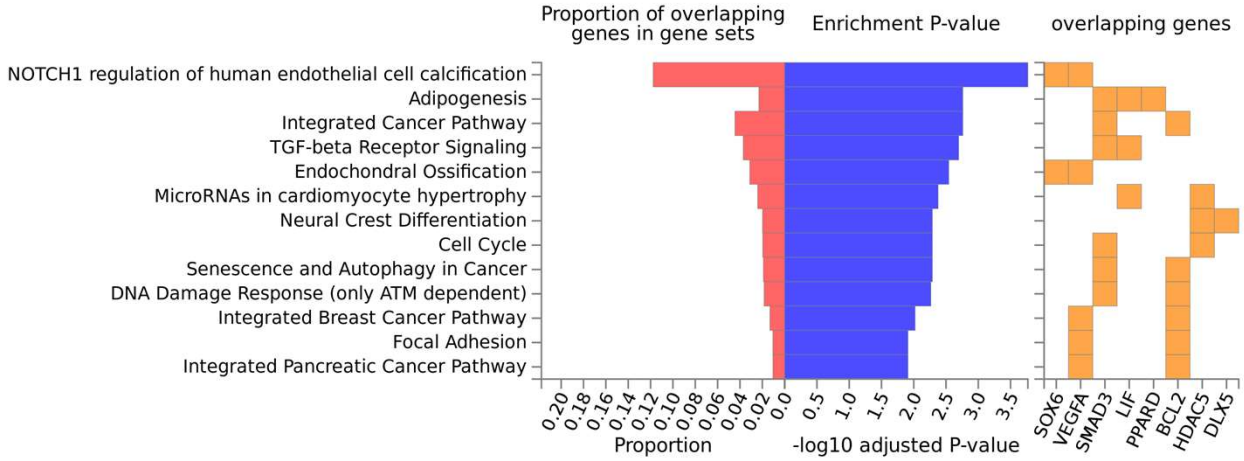

Supplementary Figure 7. WikiPathways pathway analysis results from FUMA (Watanabe *et al.* 2017, DOI: 10.1038/s41467-017-01261-5) hypergeometric testing. We tested enrichment for (**a**) genes closest to a fine-mapped SNP (n=538 genes), (**b**) genes with fine-mapped SNPs mapping to its gene body (n=287 genes), (**c**) genes with coding fine-mapped SNPs (n=39 genes), (**d**) genes mapped closest to a fine-mapped SNP which resided in an SaOS-2 ATAC-seq peak (n=62 genes), and genes identified by fine-mapped SNP was present in a (**e**) Hi-C osteoblast (n=54 genes) or (**f**) osteocyte (n=24 genes) promoter interaction peak. Well known pathways for bone biology were highlighted by FUMA, such as Wnt signalling, endochondral ossification, osteoclast and osteoblast signalling.

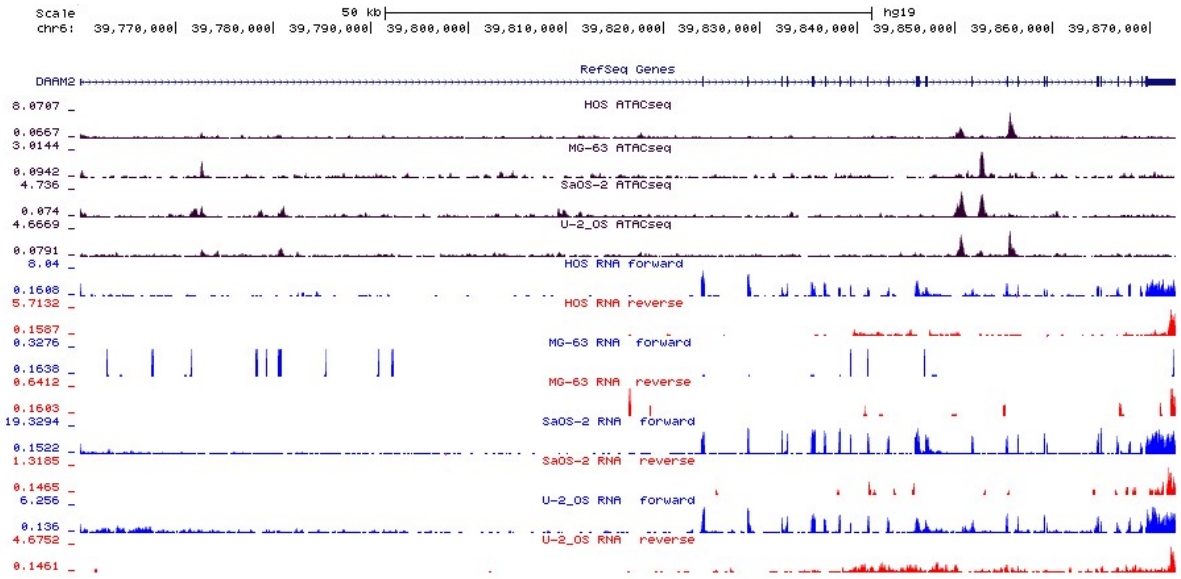

Supplementary Figure 8. Expression of *DAAM2* in osteoblast cell lines from RNA Sequencing experiments and open chromatin profiles from ATAC-seq experiments. Blue shows forward strand expression, while red shows reverse strand expression. Dark purple shows ATAC-seq open chromatin peaks. RNA of *DAAM2* is present in all cell lines, but particularly, SaOS-2, HOS and U-2_OS cell lines. RNA-seq and ATAC-seq experiments for SaOS-2, HOS, U-2_OS and MG-63 were each performed at n=1 independent experiments.

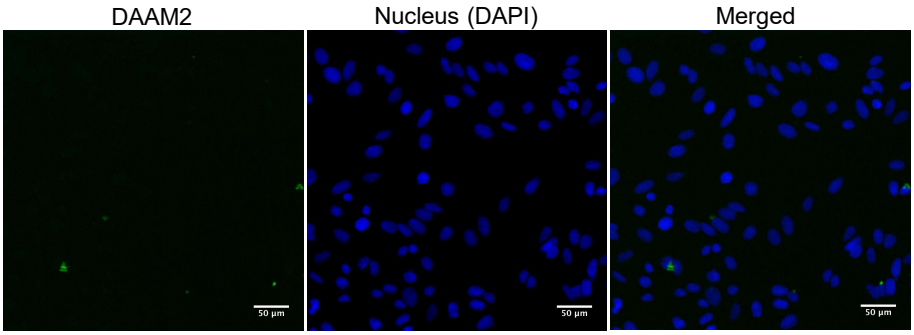

Supplementary Figure 9. No unspecific labeling of the secondary antibody in the SaOS-2 osteoblast cell line. Representative immunofluorescence of SaOS-2 cell lines stained with goat anti-rabbit IgG Alexa Fluor 488 secondary antibody (Abcam, ab150077; 1/1000), counterstained with DAPI (blue) and observed by confocal microscopy. n=2 independent experiments.

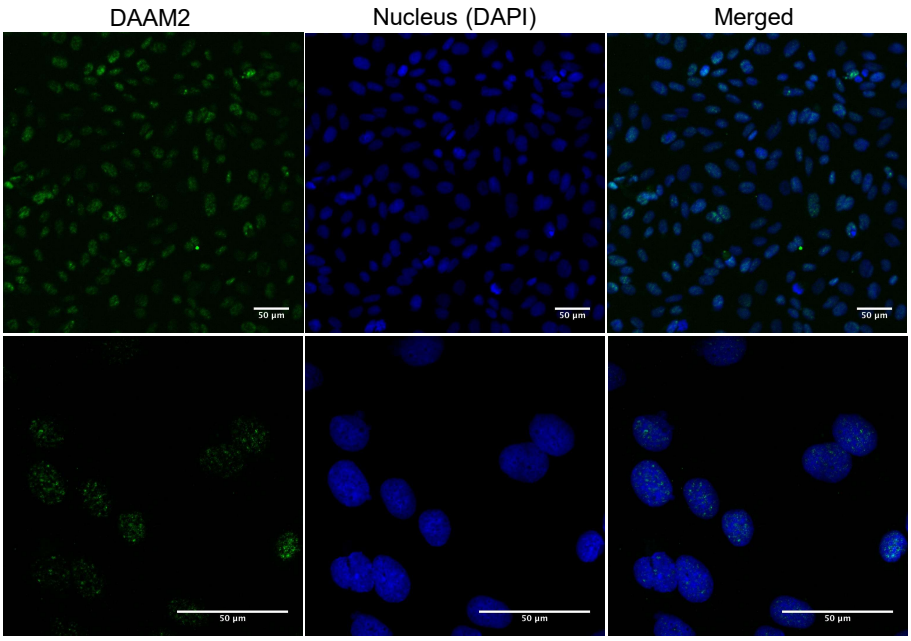

Supplementary Figure 10. DAAM2 is localized to the nucleus of SaOS-2 osteoblast cell lines. Representative immunofluorescence of SaOS-2 cell lines stained with anti-DAAM2 antibody (Sigma Aldrich, HPA051300; 1/200) followed by goat anti-rabbit IgG Alexa Fluor 488 secondary antibody (Abcam, ab150077; 1/1000), counterstained with DAPI (blue) and observed by confocal microscopy. n=6 independent experiments.

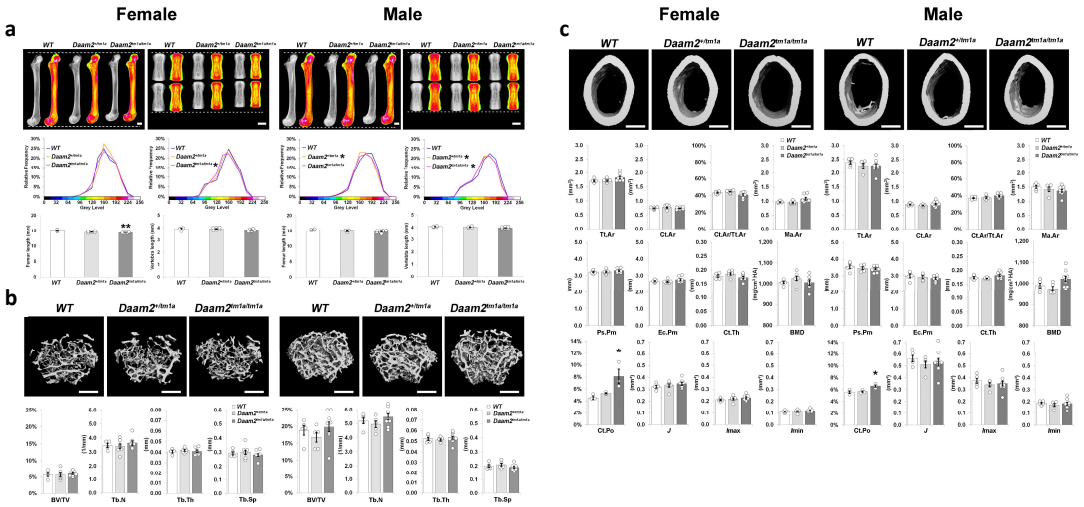

Supplementary Figure 11. Additional skeletal phenotyping of *Daam2* knockdown at postnatal day 112. a) Bone mineral content and length. X-ray microradiography images (Faxitron MX20) showing femur and caudal vertebrae from female (left) and male (right) wild-type (WT; female n=5, male=5), heterozygous (*Daam2*$^{+/tm1a}$ female n=7, male n=5) and homozygous (*Daam2*$^{tm1a/tm1a}$; female n=7, male n=9) knockout mice. Grey scale images of femur and caudal vertebrae are pseudocoloured according to a 16-colour palette in which low mineral content is green and high mineral content is pink. Relative frequency plots showing bone relative mineral content in femur and caudal vertebrae from WT, *Daam2*$^{+/tm1a}$ and *Daam2*$^{tm1a/tm1a}$ mice; (i) caudal vertebrae (female) Kolmogorov–Smirnov test WT *vs* *Daam2*^{tm1a}, D=7.05, *p<0.05; (ii) femur (male) Kolmogorov–Smirnov test WT *vs* *Daam2*$^{+/tm1a}$, D=7.83, *p<0.05 and (iii) caudal vertebrae (male) Kolmogorov–Smirnov test WT *vs Daam2*$^{+/tm1a}$, D=7.38, *p<0.05, WT *vs Daam2*$^{tm1a/tm1a}$, D=6.41, *p<0.05. Graphs demonstrate femur and caudal vertebra length in WT, *Daam2*$^{+/tm1a}$ and *Daam2*$^{tm1a/tm1a}$ mice. Data are shown as mean ± SEM; femur length (female) ANOVA p=0.0093, F=7.38, df=13, Tukey's post hoc test WT *vs Daam2*$^{tm1a/tm1a}$, **p<0.01. **b**) Trabecular bone parameters. Micro-CT images (Scanco MicroCT-50) showing proximal femur trabecular bone from WT, *Daam2*$^{+/tm1a}$, *Daam2*$^{tm1a/tm1a}$ mice. Graphs showing trabecular bone volume/tissue volume (BV/TV), trabecular number (Tb.N), trabecular thickness (Tb.Th) and trabecular spacing (Tb.Sp). Data are shown as mean ± SEM. **c**) Cortical bone parameters. Micro-CT images of mid-diaphysis cortical bone from WT, *Daam2*$^{+/tm1a}$, *Daam2*$^{tm1a/tm1a}$ mice. Graphs showing total cross-sectional area inside the periosteal envelope (Tt.Ar), cortical bone area (Ct.Ar), cortical area fraction (Ct.Ar/Tt.Ar), medullary (marrow cavity) area (M.Ar), periosteal perimeter (Ps.Pm), endocortical perimeter (Ec.Pm), cortical thickness (Ct.Th), cortical bone

mineral density (BMD), cortical porosity (Ct.Po), polar moment of inertia (*J*), maximum moment of inertia (*I*max) and minimum moment of inertia (*I*min). Data are shown as mean ± SEM; (i) cortical porosity (female) one-way ANOVA p=0.0307, F=6.58, df=8, Tukey's post hoc test WT *vs Daam2*$^{tm1a/tm1a}$, *p<0.05 and (ii) cortical porosity (male) one-way ANOVA p=0.0174, F-value=8.57, df=8, Tukey's post-hoc test WT *vs Daam2*$^{tm1a/tm1a}$, *p<0.05. Scale bars: A, 1mm, B, 0.5mm and C, 0.5mm.

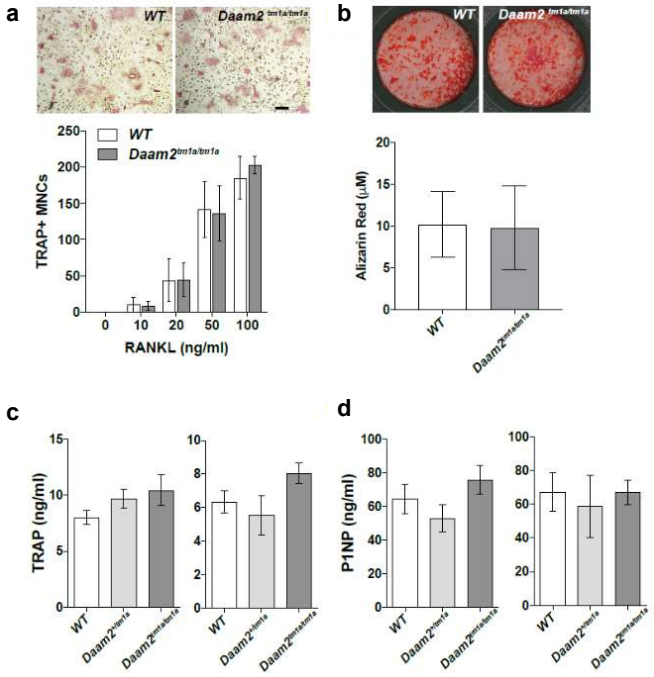

Supplementary Figure 12. Bone resorption and formation are not affected by Daam2 knockdown. a) No difference in the number of bone marrow-derived TRAP+ multinucleated cells was observed between WT and *Daam2*$^{tm1a/tm1a}$ male mice (Scale bar =100 μM, n=4, mean ± SEM). **b**) No difference was observed in the mineralization of bone marrow stromal cells between WT and *Daam2*$^{tm1a/tm1a}$ mice (n=3, mean ± SEM). No difference in bone resorption marker TRAP (**c**) and bone formation marker P1NP (**d**) was detected in the sera of WT and *Daam2*$^{tm1a/tm1a}$ mice. Data in (**c**) and (**d**) are shown as mean ± SEM, wild-type (WT; female n=5, male=5), heterozygous (*Daam2*$^{+/tm1a}$ female n=4, male n=4) and homozygous (*Daam2*$^{tm1a/tm1a}$; female n=7, male n=13) knockout mice; Females are on left and males on right.

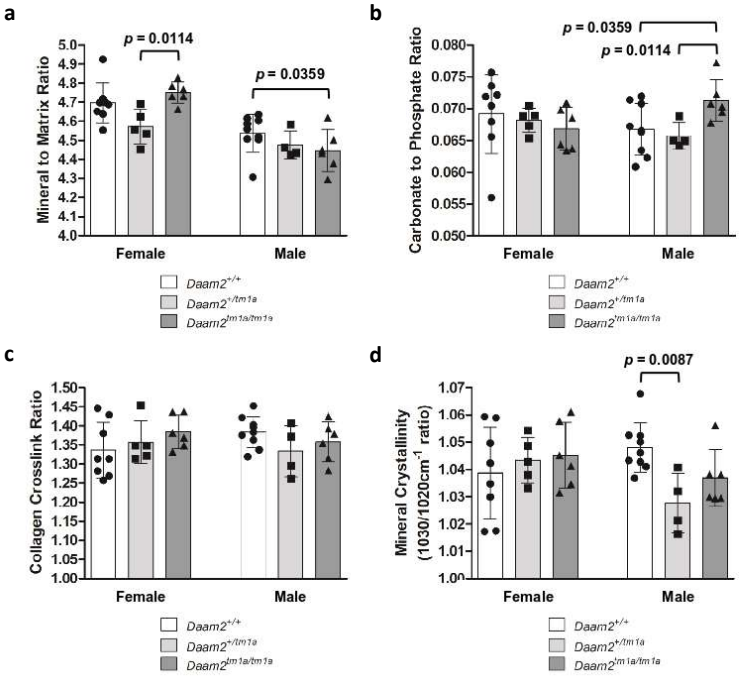

Supplementary Figure 13. Bone composition of *Daam2* transgenic and wildtype mice. Bone composition was measured in humeri from 16 week old male and female mice by Fourier Transformed Infrared Spectroscopy (FTIR). n_{males} = 8 *Daam2*$^{+/+}$ (wild-type), 4 *Daam2*$^{+/tm1a}$, 6 *Daam2*$^{tm1a/tm1a}$ and $n_{females}$ = 8 *Daam2*$^{+/+}$, 5 *Daam2*$^{+/tm1a}$, 6 *Daam2*$^{tm1a/tm1a}$. **a**) Mineral to matrix ratio was determined as the ratio of the integrated areas of the phosphate peak/amide I peak (F value, males: 4.1914, females: 5.7191). **b**) Carbonate substitution was defined as the ratio of the integrated areas of the carbonate/phosphate peaks (F value, males: 5.1126, females: 0.4464). **c**) Collagen maturity or collagen cross-linking was calculated as the ratio of the peak spectral intensities at 1660 and 1690 cm^{-1} respectively (F value, males: 1.4462, females: 1.0571). **d**) Crystallinity or crystal maturity was calculated as the ratio of the peak spectral intensities at 1030 and 1020 cm^{-1} respectively (F value, males: 6.5724, females: 0.4296). Males and females were analyzed separately due to known differences in bone between the sexes. Differences were determined by a one-way ANOVA (17 df for males and 18 df for females) and differences between individual groups determined by LS Means Tukey HSD test. The height of the bars is the mean for the sample group and error bars represent the standard deviations. A p value less than 0.05 was considered significant for the pairwise comparisons and a p value less greater than 0.05 but less than 0.06 was considered note worthy.

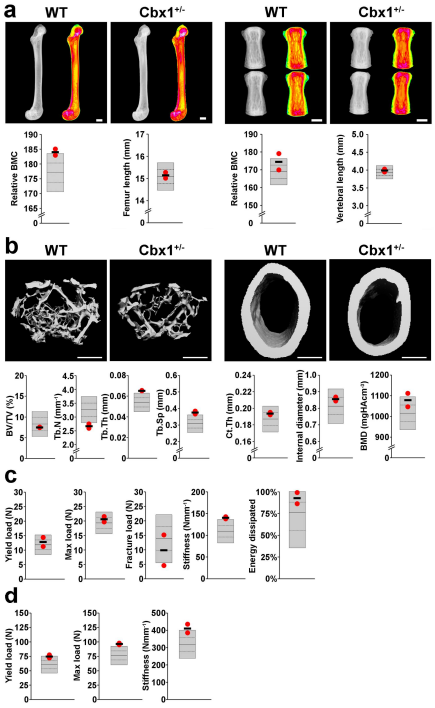

Supplementary Figure 14. Increased bone mass, stiffness and strength in adult *Chromobox 1* heterozygous deficient mice (*Cbx1*$^{+/-}$). a) X-ray microradiography images of femur and caudal vertebrae from female wild-type (WT) and *Cbx1*$^{+/-}$ mice at postnatal day 112 (P112). Graphs showing femur and caudal vertebra relative bone mineral content (BMC) and length. **b**) Micro-CT images of proximal femur trabecular bone (left) and mid-diaphysis cortical bone (right). Graphs showing trabecular bone volume/tissue volume (BV/TV), trabecular number (Tb.N), trabecular thickness (Tb.Th), trabecular spacing (Tb.Sp), cortical thickness (Ct.Th), internal cortical diameter and cortical bone mineral density (BMD). **c**) Graphs showing yield load, maximum load, fracture load, stiffness and energy dissipated prior to fracture derived from 3-point bend testing of femurs. **d**) Graphs showing yield load, maximum load and stiffness derived from compression testing of vertebrae. All graphs displayed as reference ranges derived from 320 WT mice, mean (solid line), 1.0 SD (dotted lines) and 2.0 SD (grey box). Parameters from individual mice are shown as red dots and mean values as a black line (n=2 animals). Scale bars: a, 1mm and b, 0.5mm.

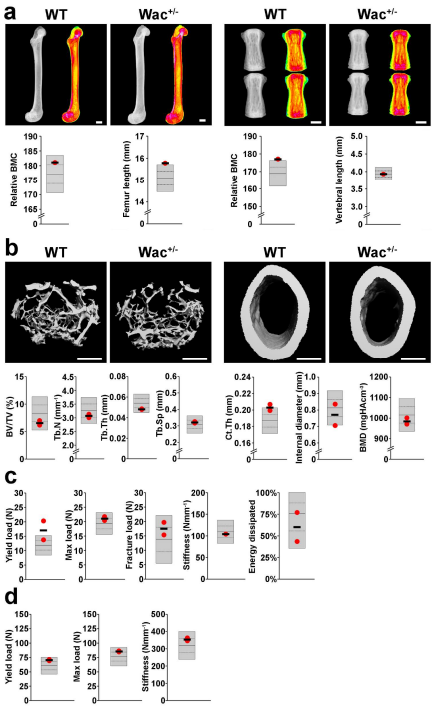

Supplementary Figure 15. Increased bone mass and strength in adult *WW Domain Containing Adaptor with Coiled-Coil* heterozygous deficient mice (*Wac*$^{+/-}$). a) X-ray microradiography images of femur and caudal vertebrae from female wild-type (WT) and *Wac*$^{+/-}$ mice at postnatal day 112 (P112). Graphs showing femur and caudal vertebra relative bone mineral content (BMC) and length. **b**) Micro-CT images of proximal femur trabecular bone (left) and mid-diaphysis cortical bone (right). Graphs showing trabecular bone volume/tissue volume (BV/TV), trabecular number (Tb.N), trabecular thickness (Tb.Th), trabecular spacing (Tb.Sp), cortical thickness (Ct.Th), internal cortical diameter and cortical bone mineral density (BMD). **c**) Graphs showing yield load, maximum load, fracture load, stiffness and energy dissipated prior to fracture derived from 3-point bend testing of femurs. **d**) Graphs showing yield load, maximum load and stiffness derived from compression testing of vertebra. All graphs displayed as reference ranges derived from 320 WT mice, mean (solid line), 1.0 SD (dotted lines) and 2.0 SD (grey box). Parameters from individual mice are shown as red dots and mean values as a black line (n=2 animals). Scale bars: a, 1mm and b, 0.5mm.

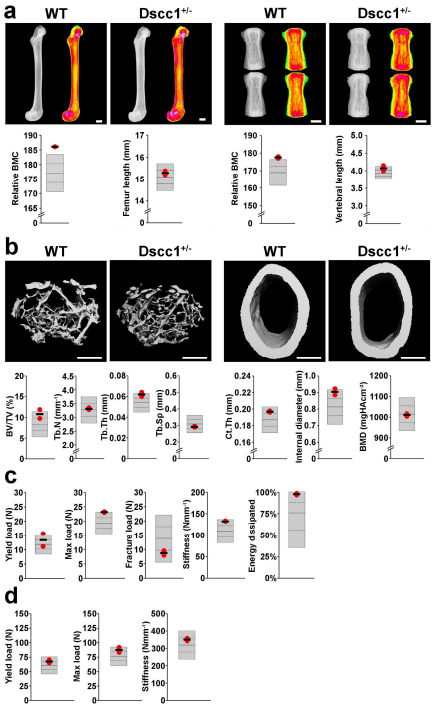

Supplementary Figure 16. Increased bone mineral content and strength in adult *DNA Replication and Sister Chromatid Cohesion 1* heterozygous deficient mice (*Dscc1*$^{+/-}$). a) X-ray microradiography images of femur and caudal vertebrae from female wild-type (WT) and *Dscc1*$^{+/-}$ mice at postnatal day 112 (P112). Graphs showing femur and caudal vertebra relative bone mineral content (BMC) and length. **b**) Micro-CT images of proximal femur trabecular bone (left) and mid-diaphysis cortical bone (right). Graphs showing trabecular bone volume/tissue volume (BV/TV), trabecular number (Tb.N), trabecular thickness (Tb.Th), trabecular spacing (Tb.Sp), cortical thickness (Ct.Th), internal cortical diameter and cortical bone mineral density (BMD). **c**) Graphs showing yield load, maximum load, fracture load, stiffness and energy dissipated prior to fracture derived from 3-point bend testing of femurs**. d**) Graphs showing yield load, maximum load and stiffness derived from compression testing of vertebrae. All graphs displayed as reference ranges derived from 320 WT mice, mean (solid line), 1.0 SD (dotted lines) and 2.0 SD (grey box). Parameters from individual mice are shown as red dots and mean values as a black line (n=2 animals). Scale bars: a, 1mm and b, 0.5mm.

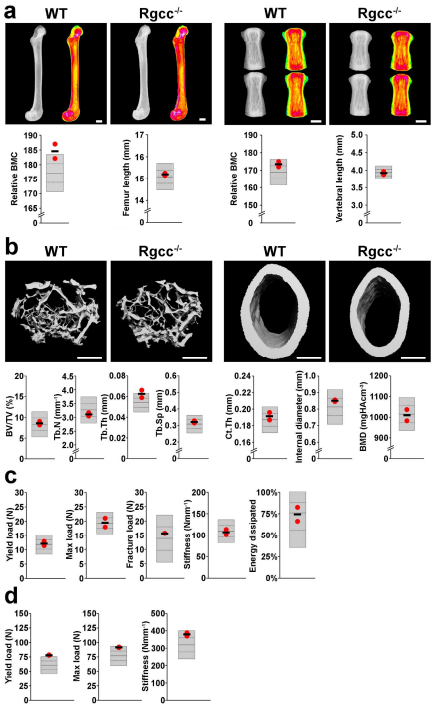

Supplementary Figure 17. Increased bone mineral content and strength in adult *DNA Regulator of Cell Cycle* knockout mice (*Rgcc*$^{-/-}$). a) X-ray microradiography images of femur and caudal vertebrae from female wild-type (WT) and *Rgcc*$^{-/-}$ mice at postnatal day 112 (P112). Graphs showing femur and caudal vertebra relative bone mineral content (BMC) and length. **b**) Micro-CT images of proximal femur trabecular bone (left) and mid-diaphysis cortical bone (right). Graphs showing trabecular bone volume/tissue volume (BV/TV), trabecular number (Tb.N), trabecular thickness (Tb.Th), trabecular spacing (Tb.Sp), cortical thickness (Ct.Th), internal cortical diameter and cortical bone mineral density (BMD). **c**) Graphs showing yield load, maximum load, fracture load, stiffness and energy dissipated prior to fracture derived from 3-point bend testing of femurs. **d**) Graphs showing yield load, maximum load and stiffness derived from compression testing of vertebrae. All graphs displayed as reference ranges derived from 320 WT mice, mean (solid line), 1.0 SD (dotted lines) and 2.0 SD (grey box). Parameters from individual mice are shown as red dots and mean values as a black line (n=2 animals). Scale bars: a, 1mm and b, 0.5mm

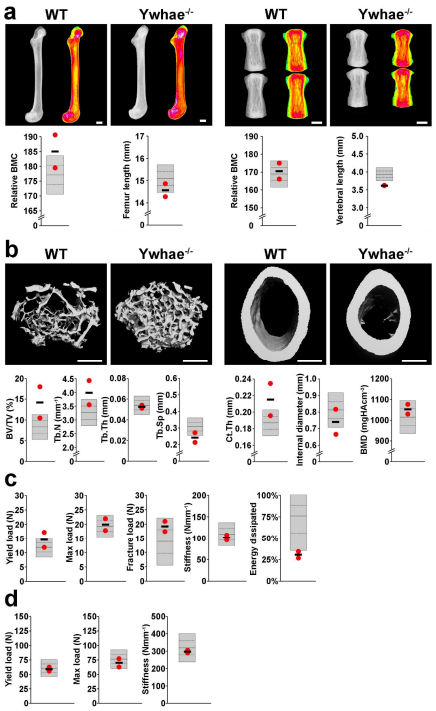

Supplementary Figure 18. Increased bone mass and brittle bones in adult *Tyrosine 3-Monooxygenase/Tryptophan 5-Monooxygenase Activation Protein Epsilon* knockout mice (*Ywhae*$^{-/-}$). **a**) X-ray microradiography images of femur and caudal vertebrae from female wild-type (WT) and *Ywhae*$^{-/-}$ mice at postnatal day 112 (P112). Graphs showing femur and caudal vertebra relative bone mineral content (BMC) and length. **b**) Micro-CT images of proximal femur trabecular bone (left) and mid-diaphysis cortical bone (right). Graphs showing trabecular bone volume/tissue volume (BV/TV), trabecular number (Tb.N), trabecular thickness (Tb.Th), trabecular spacing (Tb.Sp), cortical thickness (Ct.Th), internal cortical diameter and cortical bone mineral density (BMD). **c**) Graphs showing yield load, maximum load, fracture load, stiffness and energy dissipated prior to fracture derived from 3-point bend testing of femurs. **d**) Graphs showing yield load, maximum load and stiffness derived from compression testing of vertebrae. All graphs displayed as reference ranges derived from 320 WT mice, mean (solid line), 1.0 SD (dotted lines) and 2.0 SD (grey box). Parameters from individual mice are shown as red dots and mean values as a black line (n=2 animals). Scale bars: a, 1mm and b, 0.5mm.

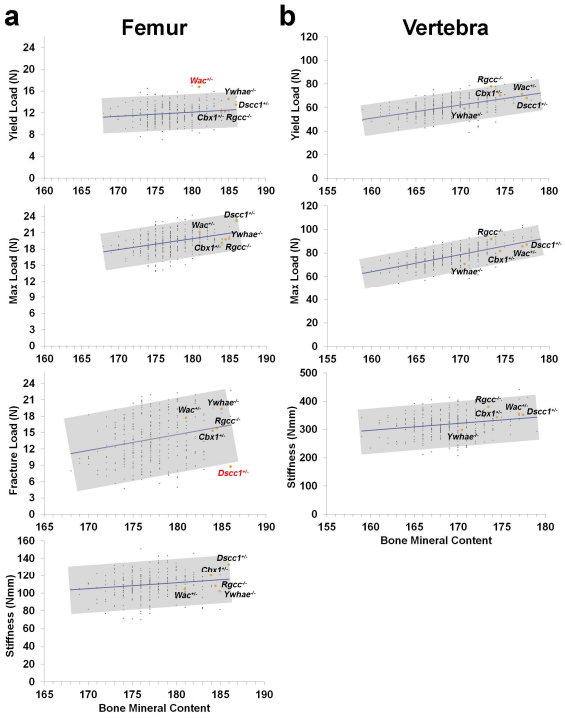

Supplementary Figure 19. Bone quality analysis from rapid throughput screening murine knockouts. a) The graphs demonstrate the relationship between bone mineral content and yield load, maximum load, fracture load and stiffness in femurs from P112 female WT mice (n=320). For yield load, maximum load, and stiffness the blue line shows the linear regression and the grey box indicates ± 2 SD. p-values were calculated from Pearson's r; (i) yield load (r=0.1561, p=0.0051); (ii) max load (r=0.3541, p=$6.96\text{x}10^{-11}$) and (iii) stiffness (r=0.1638, p=0.0033). For fracture load the blue line shows the linear regression (p=0.00003) and the grey box indicates ± 95% confidence intervals. p-values were calculated from Pearson's r; fracture load (r=0.2327, p=$2.62\text{x}10^{-5}$). The mean values for *Cbx1*$^{+/-}$, *Dscc1*$^{+/-}$, *Rgcc*$^{-/-}$, *Wac*$^{+/-}$ and *Ywhae*$^{-/-}$ [n=2 from initial OBCD screen (**Supplementary Note**)] mice are shown in orange. The *Wac*$^{+/-}$ femur yield load was 2.8 SD above the wild type reference range and *Dscc1*$^{+/-}$ fracture load was on the 1.7th centile. **b**) The graph demonstrates the relationship between bone mineral content and yield load, maximum load and stiffness in vertebrae from P112 female WT mice (n=320). For yield and maximum loads the blue line shows the linear regression and the grey box indicates ± 95% confidence intervals. p-values were calculated from Pearson's r; (i) yield load (r=0.5122, p=$8.44\text{x}10^{-23}$), and (ii) maximum load (r=0.6308, p=$6.62\text{x}10^{-37}$). For stiffness the blue line shows the linear regression and the grey box indicates ± 2 SD. p-values were calculated from Pearson's r; stiffness (r=0.2130, p=0.000123). The mean values for *Cbx1*$^{+/-}$, *Dscc1*$^{+/-}$, *Rgcc*$^{-/-}$, *Wac*$^{+/-}$ and *Ywhae*$^{-/-}$ [(n=2 from initial OBCD screen (**Supplementary Note**)] mice are shown in orange.

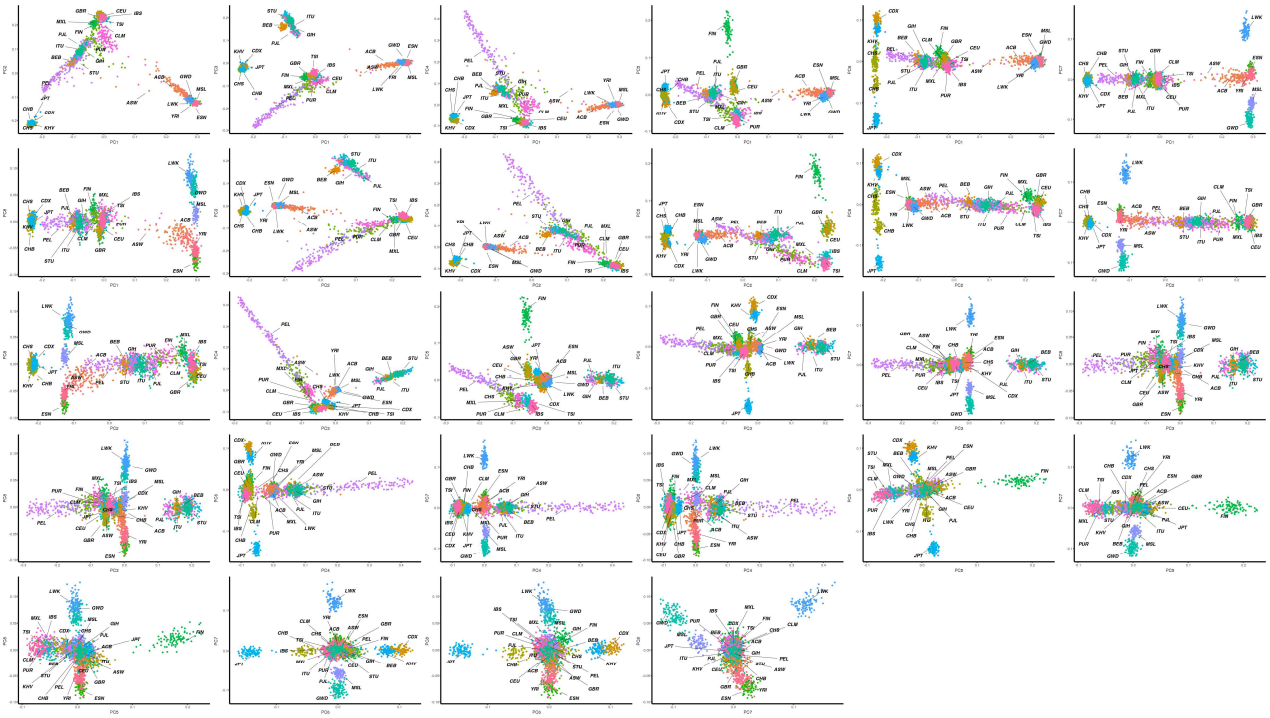

Supplementary Figure 20. Bivariate scatterplots describing pairwise comparisons of each of the first 20 ancestry informative principal components derived from unrelated subjects of the 1000 Genomes study. Data points represent subjects that are coloured according to their predefined 1000 genomes study population*. Pairwise combinations involving eigenvectors 1,2 and 5 represented the smallest number of eigenvectors that were able to adequately resolve the British sub-population (GBR) from other ethnicities and were subsequently used to for clustering and ancestry assignment of the UK Biobank sample. *CHB=Han Chinese in Beijing, China; JPT=Japanese in Tokyo, Japan; CHS=Southern Han Chinese; CDX=Chinese Dai in Xishuangbanna, China; KHV=Kinh in Ho Chi Minh City, Vietnam; CEU=Utah Residents (CEPH) with Northern and Western European Ancestry; TSI=Toscani in Italia; FIN=Finnish in Finland; GBR=British in England and Scotland; IBS=Iberian Population in Spain; YRI=Yoruba in Ibadan, Nigeria; LWK=Luhya in Webuye, Kenya; GWD=Gambian in Western Divisions in the Gambia; MSL=Mende in Sierra Leone; ESN=Esan in Nigeria; ASW=Americans of African Ancestry in SW USA; ACB=African Caribbeans in Barbados; MXL=Mexican Ancestry from Los Angeles, USA; PUR=Puerto Ricans from Puerto Rico, USA; CLM=Colombians from Medellin, Colombia; PEL=Peruvians from Lima, Peru; GIH=Gujarati Indian from Houston, USA; PJL=Punjabi from Lahore, Pakistan; BEB=Bengali from Bangladesh; STU=Sri Lankan Tamil from the UK; ITU=Indian Telugu from the UK. Sample size of the 1000G sample =2,504 and UK Biobank =486,362.

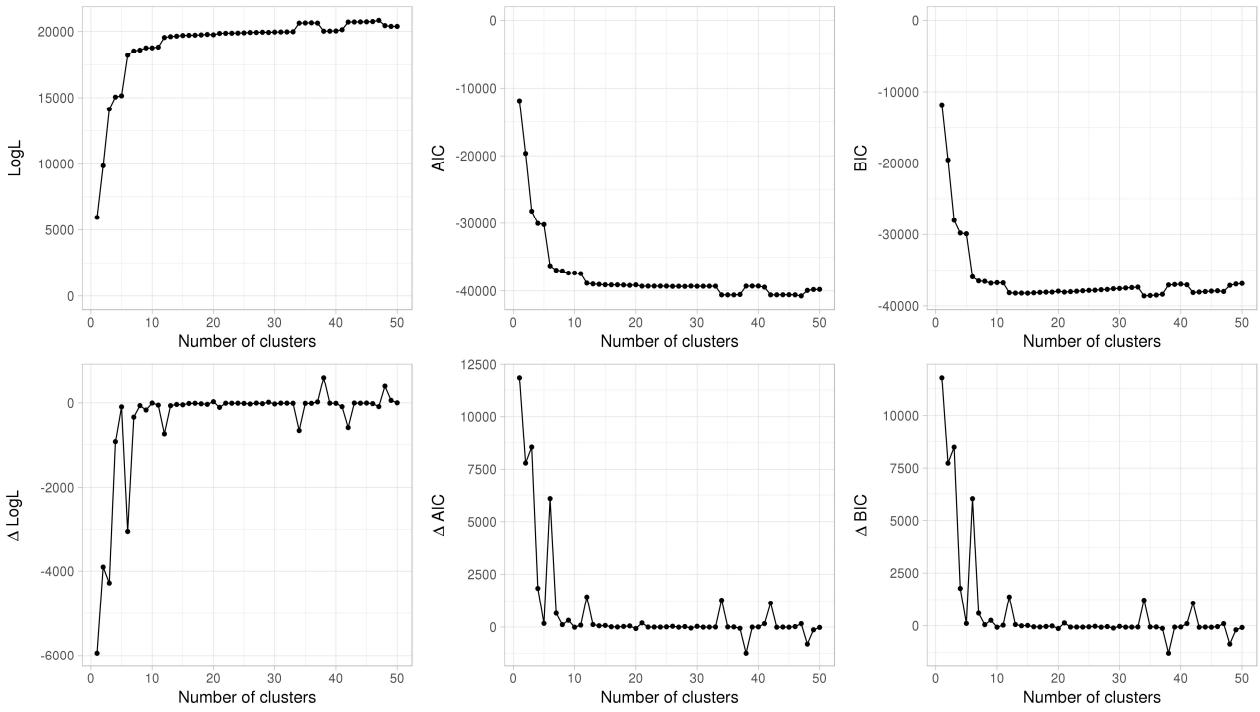

Supplementary Figure 21. Evaluating expectation maximization clustering model fit. The number of predefined clusters is described on the x-axis and model fit on the y-axis [Inferred by three model selection criteria: i.e. log-likelihood (LogL), Akaike information criteria (AIC), and Bayesian information criterion (BIC)]. Twelve predefined clusters were chosen for clustering as sensitivity analyses suggested that this number provided a good compromise between model fit and computational burden (i.e. more clusters requires more computation). Clustering involved a sample of 488,866 subjects, comprised of 2,504 1000G individuals and 486,362 UK Biobank individuals.

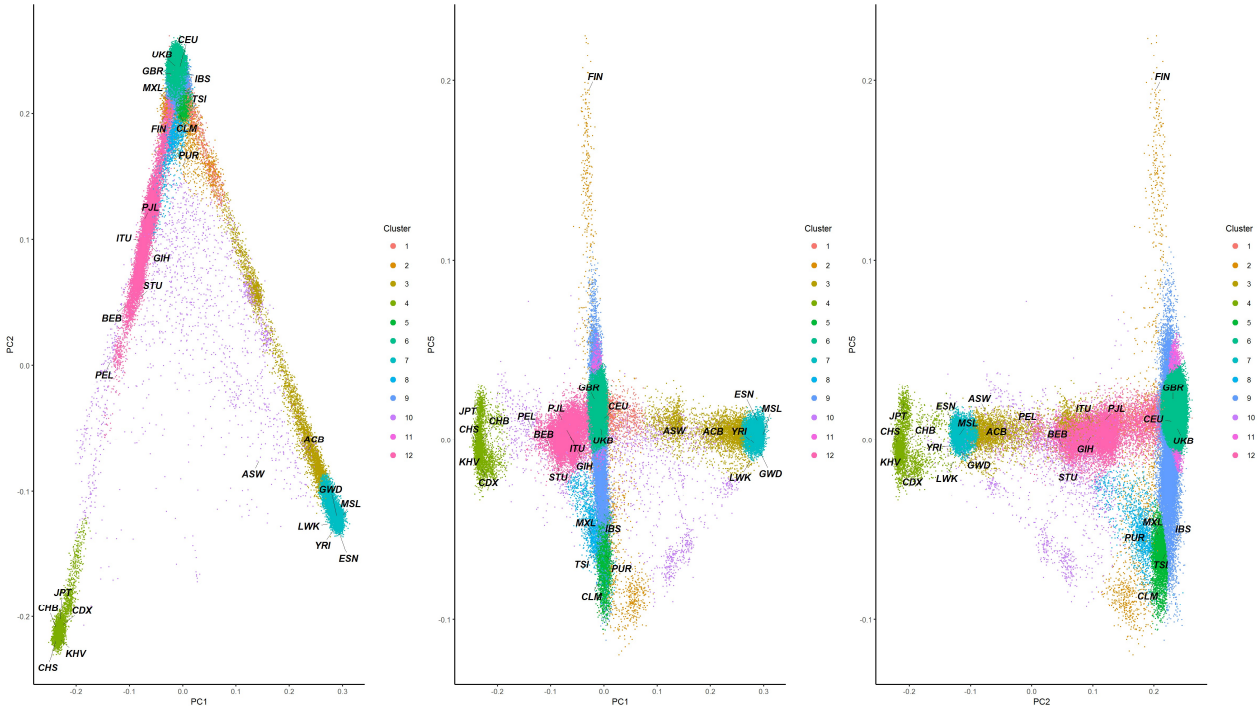

Supplementary Figure 22. Bivariate scatterplots describing pairwise comparisons of ancestry informative principal components 1,2 and 5 derived from unrelated subjects of the 1000 genomes study and all subjects from the UK Biobank sample. Data points represent subjects that are coloured according to their allocated cluster, as estimated by Expectation Maximization (EM) clustering. Samples from the UK Biobank sample are annotated using "UKB". Other 1000 genomes populations are annotated using the following: CHB=Han Chinese in Beijing, China; JPT=Japanese in Tokyo, Japan; CHS=Southern Han Chinese; CDX=Chinese Dai in Xishuangbanna, China; KHV=Kinh in Ho Chi Minh City, Vietnam; CEU=Utah Residents (CEPH) with Northern and Western European Ancestry; TSI=Toscani in Italia; FIN=Finnish in Finland; GBR=British in England and Scotland; IBS=Iberian Population in Spain; YRI=Yoruba in Ibadan, Nigeria; LWK=Luhya in Webuye, Kenya; GWD=Gambian in Western Divisions in the Gambia; MSL=Mende in Sierra Leone; ESN=Esan in Nigeria; ASW=Americans of African Ancestry in SW USA; ACB=African Caribbeans in Barbados; MXL=Mexican Ancestry from Los Angeles, USA; PUR=Puerto Ricans from Puerto Rico, USA; CLM=Colombians from Medellin, Colombia; PEL=Peruvians from Lima, Peru; GIH=Gujarati Indian from Houston, USA; PJL=Punjabi from Lahore, Pakistan; BEB=Bengali from Bangladesh; STU=Sri Lankan Tamil from the UK; ITU=Indian Telugu from the UK. Clustering involved a sample of 488,866 subjects, comprised of 2,504 1000G individuals and 486,362 individuals.

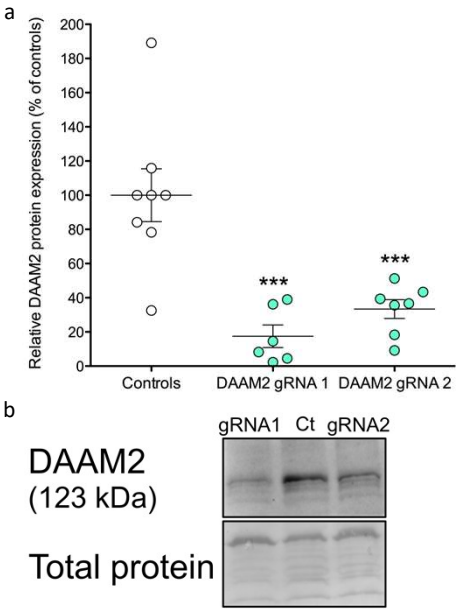

Supplementary Figure 23. Targeting DAAM2 exon 2 with CRISPR/Cas9 induced double stranded breaks reduced DAAM2 protein level in SaOS-2 cells. **a)** DAAM2 protein level quantification in control cells and edited DAAM2 cells (gRNA1 and gRNA2). Dot plot of six independent experiments ± SEM. *** represent $p=2.2x10^{-4}$ (left) and $1.3x10^{-3}$ (right) compared to control cells determined by one-way Anova ($F=15.7$, $df=2$) and Bonferroni post-hoc tests. **b)** Bands from representative Western Blots of DAAM2 (upper panel) and total protein (lower panel) of at least six independent experiments from different cell line passages. Ct: controls; gRNA1: *DAAM2* edited cells with gRNA1; gRNA2: *DAAM2* edited cells with gRNA2.

Supplementary Note

Sex heterogeneity

To investigate whether the genetic aetiology of eBMD differed between the sexes, we performed tests of sex heterogeneity across the genome. We identified 45 variants at 7 loci that displayed strong evidence of a sex difference ($p<6.6x10^{-9}$, **Supplementary Table 5**). Variants at two of these 7 loci did not reach genome-wide significance in males, females or the main eBMD GWAS, and were therefore not followed up further (**Supplementary Figure 6**, **Supplementary Table 5**). Of the five remaining loci (**Supplementary Table 5**), we detected evidence of a sex difference at *FAM9B*, a known male-only eBMD associated locus that may mediate its effect on bone through both serum testosterone levels and estradiol levels in men.[1,2] Alleles at this locus associated with increased testosterone levels were also associated with increased eBMD in males only. For the remaining loci, male-only effects were detected at *FKBP4* and *RNU6ATAC*. *FKBP4* codes for a tetratricopeptide repeat protein found in steroid receptor complexes that has been implicated in androgen receptor mediated signalling and function.[3] Variants at the *LOC105370177* (upstream of the *OPG* gene) and *ABO* loci were associated with eBMD in both sexes, but were more strongly related in males. Finally, variants within *MCM8* were associated with eBMD in females only (**Supplementary Table 6**). The same variants are known to be associated with onset of menopause[4] in the predicted direction (i.e. alleles which increase age at menopause associate with increased eBMD). Interestingly, 164 loci that reached genome-wide significance in the main analysis showed evidence of sex-heterogeneity in effect size far above expectation (164 out of 1106 SNPs had $p<0.05$, **Supplementary Table 7**). LD score regression analyses suggested that the genetic architecture influencing male and female eBMD was largely shared but that there were some significant differences between the sexes ($r_G=0.91$, SE=0.012, $p<0.001$).[5] The total number of genome-wide significant conditionally independent lead SNPs becomes 1,106 mapping to 518 loci when including our sex heterogeneity analyses, however, we focus on results from the main GWAS for the rest of our study.

Coding variants

Most genome-wide significant associations to date have arisen from non-coding variants, which has made the identification of causal genes difficult.[6] Genetic association signals at coding variation can more directly highlight a potentially causal gene. We identified 1,237 coding variants, based on the Variant Effect Predictor[7], meeting genome-wide levels of significance in their association with eBMD, prior to conditioning on other the lead SNPs in LD at each locus. This represents 1.0% of the total count of genome-wide significant variants (**Supplementary Table 8**). The average absolute effect size for coding variants was 0.025 standard deviations (interquartile range: 0.014 to 0.027), which was approximately equal to the absolute effect size for genome-wide significant common variants. These coding variants do not necessarily directly implicate a gene but may reflect non-causal associations through linkage disequilibrium with other common non-coding causal variants.

Average number of SNPs after fine-mapping loci

Prior to fine-mapping, we identified on average 235 genome-wide significant SNPs per locus. After this fine-mapping exercise, an average of two conditionally independent SNPs and five SNPs with a $\log_{10}$ Bayes factor >3 remained per locus (**Supplementary Tables 8** and **9**). The number of fine-mapped SNPs per locus ranged between 1 to 81. As a sensitivity test, we also considered a more lenient inclusion criterion for inclusion of SNPs based on a $\log_{10}$ Bayes

factor >2, which resulted in a sharp increase in the average number of SNPs per locus to 27, which in total comprised 13,742 unique SNPs (**Supplementary Table 10**).

Origins of bone and cartilage disease (OBCD) study

The Origins of Bone and Cartilage Disease (OBCD) study is determining 19 structural and functional parameters in all unselected knockout mouse lines generated at the Wellcome Trust Sanger Institute for the IKMC and IMPC. These parameters evaluate bone mineral content (BMC), 3D trabecular and cortical bone structure, bone mineralization and femoral and vertebral bone strength. To-date, the OBCD program has included the analysis of 126 knockout lines with mutations of Target Genes (**Supplementary Table 17**). Outlier phenotypes were defined as structural or strength parameters >2 standard deviations away from the reference mean, determined from over 300 age-matched, sex-matched and genetically identical C57BL/6N wild-type controls (Online Methods).

Additional in-depth characterization of DAAM2

To investigate the role of *Daam2* on bone turnover, we measured markers of bone resorption (TRAP) and formation (P1NP) in 10-week-old $Daam2^{tm1a/tm1a}$ and $Daam2^{+/tm1a}$ mice, and these did not differ from wild-type (**Supplementary Figure 12**). Furthermore, primary cultures of bone marrow mononuclear cells from $Daam2^{tm1a/tm1a}$ mice showed no difference in osteoclastogenesis, and primary osteoblast mineralization was also like wild-type (**Supplementary Figure 12**).

Male $Daam2^{tm1a/tm1a}$ mice had decreased mineral content per unit matrix protein and increased carbonate substitution (**Supplementary Figure 13**). This decrease in mineral to matrix ratio explains the overall decrease in bone mineral content observed in the absence of a decrease in cortical bone size. While bone size and geometry play a major role in controlling bone strength, decreases in mineral to matrix ratio are associated with decreased bone stiffness and decreased bending moment.[8] These decreases likely contributed to the poor bone composition and structure observed in the $Daam2^{tm1a/tm1a}$ mice.

Additional novel candidate bone genes

CBX1 encodes Chromobox 1, a highly conserved non-histone member of the heterochromatin protein family that mediates gene silencing but has no reported role in the skeleton.[9] Homozygous deletion of *Cbx1* resulted in embryonic lethality whereas adult heterozygous mice had increased bone mineral content and trabecular thickness resulting in increased stiffness and strength (**Supplementary Table 17**, **Supplementary Figure 14**). *CBX1* was identified by five SNPs with $\log_{10}$BFs >2 mapping directly to its gene body (**Supplementary Table 10**) and rs208016 (70 kbp upstream) suggested an association with fracture ($p=1.5x10^{-5}$).

WAC encodes WW Domain Containing Adaptor with Coiled-Coil, a protein of unknown function that is associated with global developmental delay and dysmorphic features in Desanto-Shinawi syndrome.[10] Homozygous deletion of *Wac* resulted in prenatal lethality whereas adult heterozygous mice had increased bone length, mass and strength (**Supplementary Table 17**, **Supplementary Figure 15**). Seven fine-mapped SNPs mapped proximally or directly to *WAC* (**Supplementary Table 10**), with two fine-mapped SNPs, rs17686203 ($\log_{10}$BF=3.1) and rs61848479 ($\log_{10}$BF=3.9) mapping to *WAC* promoter Hi-C interaction peaks in primary human osteoblasts, and for the latter SNP in primary human osteocytes (**Supplementary Table 14**). We

also identified rs17753457 (60 kbp downstream) that had a suggestive association with fracture ($p=4.3x10^{-5}$).

DSCC1 encodes DNA Replication and Sister Chromatid Cohesion 1, a component of an alternative replication factor that facilitates binding of proliferating cell nuclear antigen to DNA during S phase but has no known role in bone.[11] Homozygous knockout mice had reduced viability and adult *Dscc1*$^{+/-}$ heterozygotes had increased bone mineral content and strength (**Supplementary Table 17**, **Supplementary Figure 16**). *DSCC1* was identified by rs62526622 ($log_{10}BF=2.0$) mapping to an intronic *DSCC1* Hi-C promoter interaction peak in primary human osteoblasts. rs546691328 (180 kbp downstream) was also found to have a suggestive association with fracture ($p=2.9x10^{-4}$).

RGCC encodes Regulator of Cell Cycle, a p53 Target Gene that interacts with polo-like kinase 1, which regulates cell proliferation and apoptosis but has no documented role in the skeleton.[12] Nevertheless, *Rgcc*$^{-/-}$ knockout mice displayed increased bone mineral content and strength (**Supplementary Table 17**, **Supplementary Figure 17**). *RGCC* was identified by rs145922919 ($log_{10}BF=3.3$) mapping approximately 30 kbp upstream of *RGCC* to a Hi-C promoter interaction peak in primary human osteoblasts and rs545753481 (32 kbp upstream) also had a suggestive association with fracture ($p=3.4x10^{-3}$).

YWHAE encodes Tyrosine 3-Monooxygenase/Tryptophan 5-Monooxygenase Activation Protein, Epsilon Isoform, a pro-inflammatory cytokine that mediates signal transduction by binding to phosphoserine-containing proteins. YWHAE (14-3-3ε) binds to aminopeptidase N (CD13) to regulate chondrocyte homeostasis and has been implicated as a novel therapeutic target in osteoarthritis.[13] Rare *YWHAE* deletions have been reported in Miller-Dieker Lissencephaly syndrome which includes craniofacial abnormalities and growth retardation together with diverse neurodevelopmental abnormalities.[14] Consistent with this, homozygous deletion of *Ywhae* resulted in reduced bone length, and increased bone mass and mineral content resulting in brittle bones (**Supplementary Table 17**, **Supplementary Figure 18**). *YWHAE* was identified in our target gene approach by 22 SNPs with $log_{10}BFs >2$ (**Supplementary Table 10**) all mapping directly to *YWHAE* introns and an additional SNP, rs181451348 (1 kbp downstream) showed suggestive association with fracture ($p=7.1x10^{-5}$).

CBX1, *DSCC1*, *RGCC*, *WAC*, and *YWHAE* represent strong candidates for further in-depth functional characterization as we have performed for *DAAM2*. Bone composition and structure screens identified *WAC* and *DSCC1* as femur outliers due to *Wac*$^{+/-}$ and *Dscc1*$^{+/-}$ knockout mice being at least two standard deviations from the expected range (**Supplementary Figure 19**). Our data also support functional experiments in human cells as all five genes were expressed in all four human osteoblast cell lines we profiled with RNA-seq and ATAC-seq (Online Methods), except for *RGCC* which was highly expressed in SaOS-2 with low expression levels in U2OS, MG63, and HOS, three other human osteoblast cell lines for which we generated RNA-seq data (Online Methods). In addition, we observed suggestive association at each locus with fracture (**Supplementary Table 21**), further supporting evidence for these five genes having roles in human bone biology.

UK Biobank participant selection quality control for eBMD derivations

UK Biobank participants were initially measured at baseline (n=487,428) and had their left calcaneus (n=317,815), right calcaneus (n=4,102) or both calcanei (n=165,511) measured. A subset of these subjects was followed up at two further time points (n=20,104 and n=7,988), during which both heels were measured. A detailed description of the ascertainment procedure is provided in **Supplementary Figure 1**. Prior to quality control, ultrasound data were available for 488,683 individuals at either baseline and/or follow-up assessment. To reduce the impact of outlying measurements we first identified subjects that had both heels measured and removed those with highly discrepant (i.e. left vs. right) SOS and/or BUA measurements. To achieve this, subjects were stratified by sex and bivariate scatter plots comparing left and right heel measures of SOS and BUA were generated separately. Outliers were identified by manual inspection and removed. The same method was used to identify and remove individuals with highly discordant SOS versus BUA measured for each heel. Strict quality control was thereafter applied to male and female subjects separately using the following exclusion thresholds: SOS (Male: [≤1,450 and ≥1,750 m/s], Female [≤1,455 and ≥1,700 m/s]) and BUA (Male: [≤27 and ≥138 dB/MHz], Female [≤22 and ≥138 dB/MHz]). Individuals exceeding the threshold for SOS or BUA or both were removed from the analysis. Estimated bone mineral density (eBMD, [g/cm2]) was derived as a linear combination of SOS and BUA [eBMD=0.002592*(BUA+SOS)-3.687]. Individuals exceeding the following thresholds for eBMD were further excluded: (Male: [≤0.18 and ≥1.06 g/cm^2], Female [≤0.12 and ≥1.025 g/cm^2]). A unique list of individuals with a valid measure for the left calcaneus (n=477,380) and/or right (n=181,953) were identified separately across the three time points. Individuals with a valid right calcaneus measure were included in the final data set when no left measures were available, giving a preliminary working dataset of n=481,100, (left=475,724 and right=5,376) unique individuals. Bivariate scatter plots of eBMD, BUA and SOS were again visually inspected, and 723 additional outliers were removed, leaving a total of 480,377 valid QUS measures for SOS, BUA and BMD (264,304 females and 216,073 males).

Ancestry assignment

Genotype array data were imputed by the UK Biobank using the Haplotype Reference Consortium (HRC) panel.[15] A comprehensive description of the imputation protocol is described elsewhere.[16] A sample of 409,728 White British individuals was identified centrally by the UK Biobank, using a combination of self-reported ethnicity and genetic information. However, the reliance on self-reported information was deemed too conservative and we chose to redefine a White British sample (n=440,414) using genetic information only. We projected the UK Biobank sample onto the first 20 principal components estimated from the 1000 Genomes Phase 3 (1000G) project data[17] (where ancestry was known) using FastPCA version 2.[18] Projections used a curated set of 38,551 LD-pruned HapMap 3 Release 3 (HM3)[19] bi-allelic SNPs that were shared between the 1000G and UK Biobank datasets (MAF>1%, minor allele count >5, genotyping call rate >95%, Hardy-Weinberg p>1x10^{-6} and regions of extensive LD removed). Expectation Maximization (EM) clustering (implemented in R using EMCluster[20]) was used to compute probabilities of cluster membership based on a finite mixture of multivariate Gaussian distributions with unstructured dispersion. Eigenvectors 1, 2 and 5 were used for clustering as they represented the smallest number of eigenvectors that were able to resolve the British 1000G subpopulation (GBR) from other ethnicities (**Supplementary Figure 20**). Twelve predefined clusters were chosen for EM clustering as sensitivity analyses suggested that this number

provided a good compromise between model fit (as quantified by log likelihood, Bayesian information criterion, and Akaike information criterion) and computational burden (**Supplementary Figure 21**). UK Biobank participants (n=440,414) that clustered together with the 1000G GBR subpopulation were termed White British and used for downstream genetic analyses (**Supplementary Figure 22**).

Identification of unrelated samples for LD reference estimation and X chromosome analyses

Genome-wide complex trait analysis (GCTA)[21] was used to construct a genetic relatedness matrix (GRM) using the White British sample and a curated set of LD non-pruned HM3 autosomal genome-wide variants (n=497,687). Unrelated individuals were defined using the genome-wide relatedness measure defined by Yang *et al*.[21] where the pairwise relatedness between individuals *j* and *k* (A_{jk}) was estimated by:

$$A_{jk} = \frac{1}{N}\sum_{i=1}^{N}\frac{(x_{ij} - 2p_i)(x_{ik} - 2p_i)}{2p_i(1-p_i)}$$

where x_{ij} is the number of copies of the reference allele for the i^{th} SNP of the j^{th} and k^{th} individuals and p_i is the frequency of the reference allele across the N individuals.

Two samples of unrelated individuals were defined from the White British UK Biobank population: A sample used for X chromosome association analysis (pairwise relatedness <0.1, n=374,559) and a random sample for LD reference estimation (pairwise relatedness <0.025, n=50,000).

Fine-mapping SNPs

We used FINEMAP[22], which approximates, per input region, genotype-phenotype data with correlation matrices and summary statistics, and then implements a shotgun stochastic search algorithm to test causal configurations of SNPs rapidly and identify the most likely number of causal SNPs per signal in a Bayesian framework. We generated correlation matrices for each fine-mapped region from a subset of randomly selected 50,000 White British UK Biobank participants with the BGENIX ("URLs") and LDSTORE software.[23] FINEMAP was run with default parameters except for the number of maximum causal configurations tested, which we set to 10.[22] For the causal configuration with the highest posterior probability, each SNP was assigned a $\log_{10}$ Bayes factor as a measure of its posterior probability for being in the causal configuration. For example, if a tested region had a causal configuration of six SNPs with the highest posterior probability, all tested SNPs were assigned a Bayes factor for their marginal posterior probabilities of being in that causal configuration. Based on this information we constructed our sets of fine-mapped SNPs, including only the SNPs with the highest posterior probabilities. After testing each signal at a locus, the set of fine-mapped SNPs were collapsed into the same locus, due to the high amount of redundancy between sets for each signal, given that the approximation of genotype-phenotype data with correlation matrices and summary statistics implemented by FINEMAP is identical to GCTA-COJO.[22,24]

Target Gene pathway analysis

We used the Functional Mapping and Annotation of GWAS tool (FUMA)[25] to annotate our lists of Target Genes for their most enriched biological pathways with data from the WikiPathways[26] database. WikiPathways is an openly curated database for biological pathways

and provides information on the roles of specific genes or proteins in their respective pathways. FUMA uses WikiPathways data to compare a list of given genes against a background gene set (e.g. all protein coding genes) with hypergeometric testing. The output is then a list of enriched biological pathways based on the input gene lists. We have presented these data graphically in the **Supplementary Figure 7**.

CRISPR/Cas9 guide RNAs and PCR primers

The gRNA sequences were: gRNA 1-CAGAGGGTGGTTGTCCCGG; gRNA 2-CAGCCCCATCCCGAACGCAG; and gRNA 3-TGTCCCGGAGGTTGATTTCG.

PCR primers were designed against regions of *DAAM2* flanking the three gRNA target sequences (forward: 5′-tcctcttgtccagATCACAATG-3′ and reverse: 5′-ccaagaggagttttgagagatgga-3′) to generate an amplicon of 355 bp.

DAAM2 Western blots

To generate DAAM2 Western blots (**Supplementary Figure 23**), total protein was extracted from SaOS-2 cells using a RIPA buffer. Denatured proteins (20 µg) were separated by 10% sodium dodecylsulfate (SDS) polyacrylamide gel electrophoresis followed by transfer to nitrocellulose membranes. The membranes were blocked in 5% skim milk for one hour at room temperature followed by incubation with an anti-DAAM2 antibody (Abcam #ab169527) at 1/1,000 overnight at 4°C and the secondary antibody goat anti-rabbit IgG at 1/10,000 for one hour at room temperature (Abcam #ab205718). The band densities were quantified by densitometry using Image Lab 5.1 software (Bio-Rad). Protein levels were expressed as a ratio of protein-specific band density and that of total protein stained using MemCode Staining Solution (Thermofisher #24580). **Supplementary Figure 23** shows that DAAM2 protein expression was reduced to 17.5% and 33.5% in the gRNA1 and gRNA2 edited clones, respectively.

Rapid-throughput skeletal phenotyping

The Origins of Bone and Cartilage Disease (OBCD) study ("URLs") is undertaking rapid-throughput structural and functional skeletal phenotype analyses of all unselected knockout mice generated at the Wellcome Trust Sanger Institute as part of the International Knockout Mouse and International Mouse Phenotyping Consortia (IKMC and IMPC). Anonymized samples from 16-week-old female wild-type and mutant mice (n=2 to 6 per mutant genotype) were stored in 70% ethanol and assigned to batches for rapid throughput analysis. Mice were fed either a Breeder's Chow (Mouse Breeder Diet 5021, 21% kcal as fat, Labdiet, London, UK) or a Western diet (Western RD, 829100, 42% kcal as fat, Special Diet Services, Witham, UK) from 4 weeks of age. The relative bone mineral content and length of the femur and caudal vertebrae are determined by digital X-ray microradiography (Faxitron MX20, 10µm pixel resolution)[27–29]. Micro-CT (Scanco uCT50, 70kV, 200µA, 0.5mm aluminium filter) is used to determine trabecular parameters (bone volume BV/TV, trabecular number Tb.N, thickness Tb.Th, spacing Tb.Sp) at a 5µm voxel resolution in a 1mm region beginning 100µm proximal to the distal femoral growth plate and cortical bone parameters (thickness Ct.Th, BMD, medullary diameter) at a 10µm voxel resolution in a 1.5mm region centered in the mid-shaft region 56% along the length of the femur distal to the femoral head.[27,30,31] Biomechanical variables of bone strength and toughness (yield load, maximum load, fracture load, % energy dissipated prior to fracture) are derived from destructive 3-point bend testing of the femur and compression testing of caudal vertebra 6 and 7 (Instron 5543 load frame, 100N and 500N load cells).[27,29] Overall, 19 skeletal

parameters were reported for each individual mouse studied and compared to reference data obtained from 320 16-week-old wild-type C57BL/6 female mice. Outlier phenotypes were defined by parameters >2 standard deviations away from the reference mean determined from 320 age, sex and genetically identical C57BL/6N wild-type controls. Enrichment of outlier skeletal parameters in mice with deletion of eBMD Target Genes was determined by comparison with the frequency of outlier parameters in 526 unselected knockout lines using Fisher's Exact Test (**Supplementary Table 18,** Prism, GraphPad Software, La Jolla, USA). The 526 unselected knockout lines were generated by the WTSI and phenotyped by the OBCD program; these lines included 56 Target Genes. Five Target Genes had previously been phenotyped in an OBCD pilot study[27] and knockout lines for an additional 65 Target Genes, that had already been generated by WTSI, were prioritized for rapid-throughput skeletal phenotyping. In total, our analyses included 596 knockout lines.

Additional skeletal samples from 16-week-old WT (n=5 female, n=5 male), *Daam2*$^{+/tm1a}$ (n=7 female, n=5 male) and *Daam2*$^{tm1a/tm1a}$ (n=7 female, n=5 male) mice were analyzed as described above. Supplementary cortical bone parameters (total cross-sectional area Tt.Ar, cortical bone area Ct.Ar, medullary area M.Ar, periosteal perimeter Ps.Pm, endocortical perimeter Ec.Pm, cortical porosity Ct.Po, polar moment of inertia (*J*) and maximum and minimum moments of inertia (*I*max and *I*min)) were determined by micro-CT (at 10μm voxel resolution, except for Ct.Po which was determined at 1μm voxel resolution using the Scanco uCT50 at 70kV, 57μA, 0.5mm aluminium filter). Correlation between bone mineral content and biomechanical parameters was determined by linear regression analysis using 320 16-week-old WT femur and vertebra samples from C57BL/6 female mice. Bone composition and structure was investigated in *Daam2*$^{tm1a/tm1a}$ mice by comparing observed biomechanical parameters with values predicted by linear regression analysis of femoral and vertebral BMC and biomechanical parameters obtained from 320 WT age and sex matched controls.

RNA sequencing for mouse calvarial osteoblasts

We used whole transcriptome sequencing on mouse osteoblasts post-differentiation to obtain expression profiles of the maturing osteoblast.[32] We obtained pre-osteoblast-like cells from the neonatal calvaria of C57BL/6J mice carrying a Cyan Fluorescent Protein (*CFP*) transgene under the control of the *Col* 3.6 kbp promoter.[33] Specifically, we removed cells not expressing CFP by FACS sorting after culturing for four days in growth media. The remaining cell set was considered enriched for pre-osteoblast cells and was re-plated and subjected to an osteoblast differential cocktail, with RNA being collected every two days from days two to 18 post-differentiation. We used whole transcriptome sequencing with three technical replicates per sample and calculated a normalized expression level per gene.

In vitro osteoblast mineralization

Plastic-adherent bone marrow stromal cells (BMSCs) were isolated from 8-10 week old WT, *Daam2*$^{+/tm1a}$ and *Daam2*$^{tm1a/tm1a}$ mice as described previously. [34] Briefly, marrow cells were flushed from mouse long bones and plated in MEM containing 20% FBS in 25cm^2 tissue culture flask. Non-adherent cells were removed by medium changes 3 and 5 days later. After 7 days in culture, cells were trypsinized, scraped and re-plated at 3x10^4 cells/cm2 in 24-well plates in MEM with 10% FBS containing osteoblast differentiating factors (50 μg/ml ascorbic acid, 2.5nM dexamethasone and 10 mM β-glycerolphosphate; Sigma-Aldrich), which was added and changed every 3 days for 21 days. Cells were washed with PBS and fixed with 4%

paraformaldehyde for 15 mins then ethanol (80%) for 30 mins, rinsed and stained with 0.5% Alizarin Red (Sigma Aldrich) in water for 30 mins, washed, dried and images of the plates taken with a flat-bed scanner (model v800, Epson, North Ryde, NSW Australia). Alizarin red was then eluted with 10% cetyl pyridinium chloride (CTP; Sigma-Aldrich) in PBS overnight and quantified by measuring 562 nm absorbance (Clariostar plate reader, BMG Labtech, Offenburg, Germany) relative to standard alizarin red solutions.

In vitro assays of osteoclast formation

Osteoclasts were generated from primary BMCs flushed from mouse long bones of 8- to 10-week-old WT, *Daam2*$^{+/tm1a}$ and *Daam2*$^{tm1a/tm1a}$ mice, resuspended in MEM/FBS then added (10^5 cells/well) to 6mm diameter culture wells. These were stimulated with 10, 20, 50 and 100 ng/ml RANKL, plus 50 ng/mL M-CSF. Medium and cytokines were replaced at day 3, and on day 6 cultures were fixed with 4% paraformaldehyde and histochemically stained for TRAP using as previously described.[35] TRAP positive multinucleated cells (MNCs) containing 3 or more nuclei were counted as osteoclasts and quantified under inverted light microscopy.

Detection of serum markers of bone resorption and formation

Serum levels of bone resorption marker tartrate-resistant acid phosphatase (TRAP) and bone formation marker procollagen type 1 N-terminal propeptide (P1NP) were measured using a Rat/Mouse TRAP enzyme immunoassay kit and a Rat/Mouse P1NP enzyme immunoassay kit (Immunodiagnostic Systems, Gaithersburg, MD, USA) respectively.

Fourier-transform infrared spectroscopy

The humeri from *Daam2* WT, *Daam2*$^{+/tm1a}$ and *Daam2*$^{tm1a/tm1a}$ male and female mice were collected at 16 weeks of age. 21 male samples (11 WT, 4 *Daam2*$^{+/tm1a}$ and 6 *Daam2*$^{tm1a/tm1a}$) and 19 female samples (8 WT, 5 *Daam2*$^{+/tm1a}$ and 6 *Daam2*$^{tm1a/tm1a}$) were examined. The bones were frozen immediately and were kept at a stable temperature until analysis. All bones were processed at the same time and all analyzed on the same day to reduce batch effects. The humeri were thawed, stripped of soft tissue with epiphyses removed and the marrow cavity was flushed. Specimens were then refrozen in liquid nitrogen and pulverized at -80°C using a SPEX Sample Prep 6870 Freezer/Mill. Each sample was subjected to three rounds of pulverization at 15 cycles per second for one minute with a two-minute cool-down between each round. The samples were lyophilized under vacuum at -51°C overnight to ensure they were completely dehydrated. Anhydrous potassium bromide (KBr) was then added until the final concentration of bone in the samples was between 2.50-2.56% by mass. KBr pellets were formed by compressing 20 mg of mixed KBr and bone samples in a 7 mm die under 4 tons of force. The formed pellets were loaded into a Nicolet iS50 FT-IR spectrophotometer (Thermo Fisher Scientific). The collection chamber was continuously purged with dry nitrogen gas to minimize noise from moisture and carbon dioxide. Background noise was collected on KBr-only pellets and subtracted at the beginning of each cohort or after 30min of continuous measurements (whichever occurred first). For each sample, 128 scans between 400-2200 cm^{-1} (wave numbers) were collected at a resolution of 4.0cm^{-1} using Happ-Genzel apodization. The wave number data was curve fit to absorbance, with baselining and spectral analyses performed using custom algorithms and scripts written in the R programming language (R version 3.4.2). The scripts were built on top of the ChemoSpec (version 4.2.8) and MESS (version 0.3-2) packages. Local minima were used as limits of integration to calculate areas under the curve for the carbonate,

phosphate and amide I peaks; the mineral to matrix ratio, carbonate to phosphate ratio were then calculated using these areas in the appropriate ratios. Collagen maturity and crystallinity were calculated from the spectral data using absorbance values at literature-reported and validated wavenumbers.[36] Between two and four technical replicates were run for each sample, based on the amount of material available. Two samples (both from WT males) were removed from all subsequent statistical analyses as the signal to noise ratio was excessive for the spectral data for all technical replicates, thus precluding obtaining meaningful information from those samples. Values for technical replicates where averaged for each specimen. Differences between genotypes were determined by one-way ANOVA, followed by a Tukey's post-hoc test. Data from male and female mice were analyzed separately.

References

1. Eriksson, A. L. *et al.* Genetic Determinants of Circulating Estrogen Levels, and Evidence of a Causal Effect of Estradiol on Bone Density in Men. *J. Clin. Endocrinol. Metab.* (2018). doi:10.1210/jc.2017-02060
2. Ohlsson, C. *et al.* Genetic determinants of serum testosterone concentrations in men. *PLoS Genet.* **7,** e1002313 (2011).
3. Yong, W. *et al.* Essential role for co-chaperone Fkbp52 but not Fkbp51 in androgen receptor-mediated signaling and physiology. *J. Biol. Chem.* **282,** 5026–5036 (2007).
4. He, C. *et al.* Genome-wide association studies identify loci associated with age at menarche and age at natural menopause. *Nat. Genet.* **41,** 724–728 (2009).
5. Bulik-Sullivan, B. *et al.* An atlas of genetic correlations across human diseases and traits. *Nat. Genet.* **47,** 1236–1241 (2015).
6. Timpson, N. J., Greenwood, C. M. T., Soranzo, N., Lawson, D. J. & Richards, J. B. Genetic architecture: The shape of the genetic contribution to human traits and disease. *Nat. Rev. Genet.* **19,** 110–124 (2018).
7. McLaren, W. *et al.* The Ensembl Variant Effect Predictor. *Genome Biol.* **17,** 122 (2016).
8. Donnelly, E., Chen, D. X., Boskey, A. L., Baker, S. P. & Van Der Meulen, M. C. H. Contribution of mineral to bone structural behavior and tissue mechanical properties. *Calcif. Tissue Int.* **87,** 450–460 (2010).
9. Bannister, A. J. *et al.* Selective recognition of methylated lysine 9 on histone H3 by the HP1 chromo domain. *Nature* **410,** 120–124 (2001).
10. De Santo, C. *et al.* WAC loss-of-function mutations cause a recognisable syndrome characterised by dysmorphic features, developmental delay and hypotonia and recapitulate 10p11.23 microdeletion syndrome. *J. Med. Genet.* **52,** 754–761 (2015).
11. Bermudez, V. P. *et al.* The alternative Ctf18-Dcc1-Ctf8-replication factor C complex required for sister chromatid cohesion loads proliferating cell nuclear antigen onto DNA. *Proc. Natl. Acad. Sci.* **100,** 10237–10242 (2003).
12. Saigusa, K. *et al.* RGC32, a novel p53-inducible gene, is located on centrosomes during mitosis and results in G2/M arrest. *Oncogene* **26,** 1110–1121 (2007).
13. Nefla, M. *et al.* The pro-inflammatory cytokine 14-3-3 is a ligand of CD13 in cartilage. *J. Cell Sci.* **128,** 3250–3262 (2015).
14. Nagamani, S. C. S. *et al.* Microdeletions including YWHAE in the Miller-Dieker syndrome region on chromosome 17p13.3 result in facial dysmorphisms, growth restriction, and cognitive impairment. *J. Med. Genet.* **46,** 825–833 (2009).
15. McCarthy, S. *et al.* A reference panel of 64,976 haplotypes for genotype imputation. *Nat. Genet.* **48,** 1279–1283 (2016).
16. Bycroft, C. *et al.* Genome-wide genetic data on ~500,000 UK Biobank participants. *bioRxiv* https://doi.org/10.1101/166298 (2017). doi:10.1101/166298
17. Auton, A. *et al.* A global reference for human genetic variation. *Nature* **526,** 68–74 (2015).
18. Galinsky, K. J. *et al.* Fast Principal-Component Analysis Reveals Convergent Evolution of ADH1B in Europe and East Asia. *Am. J. Hum. Genet.* **98,** 456–472 (2016).
19. Altshuler, D. M. *et al.* Integrating common and rare genetic variation in diverse human populations. *Nature* **467,** 52–58 (2010).
20. Chen, W.-C. & Maitra, R. EM Algorithm for Model-Based Clustering of Finite Mixture Gaussian Distribution. R package (2015).

21. Yang, J., Lee, S. H., Goddard, M. E. & Visscher, P. M. GCTA: A tool for genome-wide complex trait analysis. *Am. J. Hum. Genet.* **88,** 76–82 (2011).
22. Benner, C. *et al.* FINEMAP: Efficient variable selection using summary data from genome-wide association studies. *Bioinformatics* **32,** 1493–1501 (2016).
23. Benner, C. *et al.* Prospects of Fine-Mapping Trait-Associated Genomic Regions by Using Summary Statistics from Genome-wide Association Studies. *Am. J. Hum. Genet.* **101,** 539–551 (2017).
24. Yang, J. *et al.* Conditional and joint multiple-SNP analysis of GWAS summary statistics identifies additional variants influencing complex traits. *Nat. Genet.* **44,** 369–375 (2012).
25. Watanabe, K., Taskesen, E., Van Bochoven, A. & Posthuma, D. Functional mapping and annotation of genetic associations with FUMA. *Nat. Commun.* **8,** 1826 (2017).
26. Kutmon, M. *et al.* WikiPathways: Capturing the full diversity of pathway knowledge. *Nucleic Acids Res.* **44,** D488–D494 (2016).
27. Bassett, J. H. D. *et al.* Rapid-Throughput Skeletal Phenotyping of 100 Knockout Mice Identifies 9 New Genes That Determine Bone Strength. *PLoS Genet.* **8,** e1002858 (2012).
28. Bassett, J. H. D., Van Der Spek, A., Gogakos, A. & Williams, G. R. Quantitative X-ray imaging of rodent bone by faxitron. *Methods Mol. Biol.* **816,** 499–506 (2012).
29. Bassett, J. H. D. *et al.* Optimal bone strength and mineralization requires the type 2 iodothyronine deiodinase in osteoblasts. *Proc. Natl. Acad. Sci.* **107,** 7604–7609 (2010).
30. Esapa, C. T. *et al.* Bone Mineral Content and Density. *Curr. Protoc. Mouse Biol.* **2,** 365–400 (2012).
31. Bassett, J. H. D. *et al.* Thyrostimulin regulates osteoblastic bone formation during early skeletal development. *Endocrinology* **156,** 3098–3113 (2015).
32. Kemp, J. P. *et al.* Identification of 153 new loci associated with heel bone mineral density and functional involvement of GPC6 in osteoporosis. *Nat. Genet.* **49,** 1468–1475 (2017).
33. Kalajzic, I. *et al.* Expression profile of osteoblast lineage at defined stages of differentiation. *J. Biol. Chem.* **280,** 24618–24626 (2005).
34. Lee, N. J. *et al.* Critical role for Y1 receptors in mesenchymal progenitor cell differentiation and osteoblast activity. *J. Bone Miner. Res.* **25,** 1736–1747 (2010).
35. Quinn, J. M. W. *et al.* Calcitonin receptor antibodies in the identification of osteoclasts. *Bone* **25,** 1–8 (1999).
36. Gourion-Arsiquaud, S., West, P. A. & Boskey, A. L. Fourier transform-infrared microspectroscopy and microscopic imaging. *Methods Mol. Biol.* **455,** 293–303 (2008).